Journal of the Atmospheric Sciences

Diagnosis of Middle Atmosphere Climate Sensitivity by the Climate Feedback Response Analysis Method

--Manuscript Draft--

Manuscript Number:	
Full Title:	Diagnosis of Middle Atmosphere Climate Sensitivity by the Climate Feedback Response Analysis Method
Article Type:	Article
Corresponding Author:	Xun Zhu Johns Hopkins University Laurel, UNITED STATES
Corresponding Author's Institution:	Johns Hopkins University
First Author:	Xun Zhu
Order of Authors:	Xun Zhu
	Jeng-Hwa Yee
	Ming Cai
	William H. Swartz
	Lawrence Coy
	Valentina Aquila
	Elsayed R. Talaat
Abstract:	We present a new method to diagnose the middle atmosphere climate sensitivity by extending the Climate Feedback-Response Analysis Method (CFRAM) for the coupled atmosphere-surface system to the middle atmosphere. The Middle atmosphere CFRAM (MCFRAM) is built on the atmospheric energy equation per unit mass with radiative heating and cooling rates as its major thermal energy sources. MCFRAM preserves the CFRAM unique feature of an additive property for which the sum of all partial temperature changes due to variations in external forcing and feedback processes equals the observed temperature change. In addition, MCFRAM establishes a physical relationship of radiative damping between the energy perturbations associated with various feedback processes and temperature perturbations associated with thermal responses. MCFRAM is applied to both measurements and model output fields to diagnose the middle atmosphere climate sensitivity. It is found that the largest component of the middle atmosphere temperature response to the 11-year solar cycle (solar maximum vs. solar minimum) is directly from the partial temperature change due to the variation of the input solar flux. Increasing CO2 always cools the middle atmosphere with time whereas partial temperature change due to O3 variation could be either positive or negative. The partial temperature changes due to different feedbacks show distinctly different spatial patterns. The thermally driven globally averaged partial temperature change due to all radiative processes is approximately equal to the observed temperature change, ranging from −0.5 K near 25 km to −1.0 K near 70 km from the near solar maximum to the solar minimum.
Suggested Reviewers:	Roland Garcia rgarcia@ucar.edu
	K. K. Tung tung@amath.washington.edu
	Paul Newman Paul.A.Newman@nasa.gov
	Steven Pawson steven.pawson-1@nasa.gov
	Brian Soden

	bsoden@rsmas.miami.edu

Diagnosis of Middle Atmosphere Climate Sensitivity by the Climate Feedback Response Analysis Method

Xun Zhu[1], Jeng-Hwa Yee[1], Ming Cai[2], William H. Swartz[1], Lawrence Coy[3], Valentina Aquila[4], and Elsayed R Talaat[5]

[1] The Johns Hopkins University Applied Physics Laboratory, 11100 Johns Hopkins Road, Laurel, MD 20723
[2] Department of Earth, Ocean and Atmospheric Science, The Florida State University, Tallahassee, FL 21218
[3] Science Systems and Applications, Inc, 10210 Greenbelt Road, Lanham, MD 20706
[4] GESTAR/Johns Hopkins University, 3400 N Charles Street, Baltimore, MD 21218
[5] Heliophysics Division, NASA Headquarters, Washington, D.C. 20546

Submitted to *Journal of the Atmospheric Sciences*

August 26, 2014

Corresponding author address:

Dr. Xun Zhu
The Johns Hopkins University
Applied Physics Laboratory
11100 Johns Hopkins Road
Laurel, MD 20723-6099
Phone: 443-778-8764
Fax: 443-778-6670
E-mail: xun.zhu@jhuapl.edu

Abstract

We present a new method to diagnose the middle atmosphere climate sensitivity by extending the Climate Feedback-Response Analysis Method (CFRAM) for the coupled atmosphere-surface system to the middle atmosphere. The Middle atmosphere CFRAM (MCFRAM) is built on the atmospheric energy equation per unit mass with radiative heating and cooling rates as its major thermal energy sources. MCFRAM preserves the CFRAM unique feature of an additive property for which the sum of all partial temperature changes due to variations in external forcing and feedback processes equals the observed temperature change. In addition, MCFRAM establishes a physical relationship of radiative damping between the energy perturbations associated with various feedback processes and temperature perturbations associated with thermal responses. MCFRAM is applied to both measurements and model output fields to diagnose the middle atmosphere climate sensitivity. It is found that the largest component of the middle atmosphere temperature response to the 11-year solar cycle (solar maximum vs. solar minimum) is directly from the partial temperature change due to the variation of the input solar flux. Increasing CO_2 always cools the middle atmosphere with time whereas partial temperature change due to O_3 variation could be either positive or negative. The partial temperature changes due to different feedbacks show distinctly different spatial patterns. The thermally driven globally averaged partial temperature change due to all radiative processes is approximately equal to the observed temperature change, ranging from −0.5 K near 25 km to −1.0 K near 70 km from the near solar maximum to the solar minimum.

1. Introduction

The warming of Earth's surface and lower atmosphere is associated with enhanced middle atmosphere cooling and a strengthening of the Brewer-Dobson circulation through radiative, dynamical, and photochemical coupling. Because both the air density and the optical depths of major radiatively active species decrease with altitude, the physical state of the middle atmosphere as represented by various parameters such as temperature and winds is quite sensitive to climate forcing and is thus a good indicator of surface global warming. Hence, a more accurate quantification of the middle atmosphere responses to solar variability and anthropogenic changes in trace species is necessary to improve predictions of climate change.

The Climate Feedback–Response Analysis Method (CFRAM) has been developed for separating and estimating various climate feedbacks in the coupled troposphere-ocean system (Lu and Cai 2009; Cai and Lu 2009; hereafter LC09 and CL09). CFRAM is formulated based on the atmosphere-surface energy equation, and it explicitly decomposes the directly *measurable* total temperature change into partial temperature changes due to individual external forcing and feedback processes (LC09, CL09). The unique feature of CFRAM is that this decomposition into partial temperature changes is locally *additive*, so that the total temperature change is the sum of all the partial temperature changes at every spatial point. From the modeling perspective, the so-called external forcing and its variation of a system are akin to independent variables or parameters that would be prescribed as input values in a model. On the other hand, the feedback or internal processes of a system are similar to dependent variables or parameters that often constitute a set of model output values.

In this paper, CFRAM is extended to the middle atmosphere based on three physical features of this region: (i) radiative energy exchange plays a major role in the energy budget; (ii) the air density varies with altitude by several orders of magnitude and the energy deposition per unit mass is often scaled by a factor that slowly varies with altitude or log-pressure; and (iii) the energy flux associated with the level of the Earth's surface and the layered middle atmosphere

are not directly coupled. As a result, the Middle atmosphere Climate Feedback–Response Analysis Method (MCFRAM) is formulated by the energy equation in a form of heating and cooling rates per unit mass in a commonly used unit of $\mathrm{K\ day^{-1}}$. Its mathematical form is similar to a well-documented radiative transfer technique for analyzing radiative damping or relaxation of the atmospheric temperature disturbances (*e.g.*, Goody and Yung 1989, Zhu and Strobel 1991). The newly developed MCFRAM is here applied to the middle atmosphere to derive various partial temperature changes based on both satellite measurements and output of a three-dimensional (3D) chemistry-climate model (CCM).

In Section 2, we briefly review and extend CFRAM to the middle atmosphere. Then, we perform the fundamental eigenmode analysis to the generalized damping matrix derived from the MCFRAM. The middle atmosphere temperature and ozone fields needed in the analysis are derived from the Sounding of the Atmosphere using Broadband Emission Radiometer (SABER) onboard the Thermosphere, Ionosphere Mesosphere, Energetics and Dynamics (TIMED) satellite. Section 3 shows the MCFRAM results derived from the SABER measurements whereas section 4 performs a set of similar MCFRAM analyses on the output fields of the Goddard Earth Observing System chemistry-climate model (GEOSCCM; Pawson *et al.*, 2008, and references therein). Section 5 summarizes the paper.

2. Review and extension of the Coupled Feedback Response Analysis Method

2.1 Formulation of the middle atmosphere CFRAM

CFRAM was originally formulated in a form of a vertical energy flux difference for a single-column energy equation in a form of the time mean energy balance equation (LC09; CL09):

$$\mathbf{R}^*(\mathbf{T}, r, s, ..., \alpha, \beta, ...) = \mathbf{S}^*(\mathbf{T}, r, s, ..., \alpha, \beta, ...) + \mathbf{Q}^*(\mathbf{T}, r, s, ..., \alpha, \beta, ...), \quad (1)$$

where $\mathbf{R}^*$ and $\mathbf{S}^*$ are the infrared and solar flux differences corresponding to total radiative cooling and heating of a layered atmosphere, respectively. $\mathbf{Q}^*$ is the non-radiative energy flux

convergence in the atmospheric layers. **T** is temperature profile, (r, s, …) are the mixing ratios of radiatively active species such as CO_2, O_3, H_2O and clouds, and (α, β, …) are the parameters such as the solar irradiance, surface albedo and solar declination angle that will affect the atmospheric energy. The terms in the energy Eq. (1) for CFRAM have the units of energy flux $\mathrm{W\,m^{-2}}$, which corresponds to the heating or the cooling rate per unit volume for a given layer of atmosphere. There are several advantages of adopting the flux form with units $\mathrm{W\,m^{-2}}$ in the classic CFRAM: (i) the energy flux of the atmosphere can be naturally coupled with the surface energy flux; (ii) the top of the atmosphere (TOA) version of CFRAM can be directly compared to a TOA-based climate feedback analysis such as the partial radiative perturbation (PRP) method; (iii) the layer thickness of the tropospheric CCMs is usually slowly varying in mass so the heating or cooling rate perturbations per unit space of different layers also slowly vary with altitude.

The air density decreases with altitude exponentially in the middle atmosphere, ranging from the tropopause (~10 km) to the turbopause (~110 km), spanning several orders of magnitude in density variation. The energy deposition or the atmospheric heating rate in measurements and models is often scaled in a unit mass with a setting in vertical grid that slowly varies with altitude or log-pressure. As a result, we begin by developing our MCFRAM from an energy equation per unit mass, *i.e.*, by dividing Eq. (1) by $c_p\rho\Delta z$ with c_p, ρ and Δz being the specific heat at constant pressure, air density and layer thickness, respectively,

$$\mathbf{R}(\mathbf{T}, r, s, ..., \alpha, \beta, ...) = \mathbf{S}(\mathbf{T}, r, s, ..., \alpha, \beta, ...) + \mathbf{Q}(\mathbf{T}, r, s, ..., \alpha, \beta, ...) + \mathbf{Q}_{mol}(\mathbf{T}), \quad (2)$$

where **R** and **S** are the radiative cooling and heating rates, respectively. **Q** is the non-radiative heating rate excluding the molecular thermal conductivity $\mathbf{Q}_{mol}(\mathbf{T})$ that is only a function of temperature profile **T** (Banks and Kockarts 1973). The units of all terms in Eq. (2) are $\mathrm{K\,day^{-1}}$. We now consider two statistical equilibrium states 1 and 2 with two different sets of corresponding atmospheric parameters all satisfying the energy balance equation (2). In practice,

these two states can be two ensemble, time or spatially averaged mean states. The difference of the energy equations between these two states is

$$\Delta(\mathbf{R}-\mathbf{Q}_{mol})=\Delta\mathbf{S}+\Delta\mathbf{Q}\,. \tag{3}$$

We now introduce the linear approximation to the responses of $\mathbf{R}$ and $\mathbf{Q}_{mol}$ to the temperature variation and separate this term from the variations due to other parameters:

$$\Delta(\mathbf{R}-\mathbf{Q}_{mol})\approx\frac{\partial(\mathbf{R}-\mathbf{Q}_{mol})}{\partial\mathbf{T}}\Delta\mathbf{T}+[\mathbf{R}(\overline{\mathbf{T}},r_2,s_2,...,\alpha_2,\beta_2,...)-\mathbf{R}(\overline{\mathbf{T}},r_1,s_1,...,\alpha_1,\beta_1,...)]\,, \tag{4}$$

where $\overline{\mathbf{T}}$ is the "mean temperature profile" between profiles $\mathbf{T}_1$ and $\mathbf{T}_2$. Substituting Eq. (4) into Eq. (3), we obtain

$$\Delta\mathbf{T}=\mathbf{A}^{-1}\left\{\Delta\mathbf{S}-\Delta'\mathbf{R}+\Delta\mathbf{Q}\right\}, \tag{5}$$

where $\mathbf{A}\equiv\partial(\mathbf{R}-\mathbf{Q}_{mol})/\partial\mathbf{T}\approx\Delta(\mathbf{R}-\mathbf{Q}_{mol})/\Delta\mathbf{T}$ is the generalized damping matrix in units of day^{-1} and $\Delta'\mathbf{R}$ defined by the last two terms in Eq. (4) is the change in total cooling rate due to all parameters except the temperature profile.

In CFRAM, where the surface and the atmosphere are strongly coupled radiatively and dynamically, the discretization of the energy equation (1) and the derivation of the "Planck feedback matrix" $\partial\mathbf{R}^{*}\partial\mathbf{T}$ based on the temperature profile need to include the temperatures of both the surface level and layers of the atmosphere (LC09). The surface temperature and atmospheric temperature are treated as equally important in the setting of the problem. As a result, Eq. (1) needs to be in the form of energy flux divergence in units of energy flux W m^{-2}. The temperature profile in the middle atmosphere is not directly coupled to the Earth surface. It can therefore be discretized solely based on a layered atmosphere in an energy equation of unit mass (Eq. 2). The effect of the energy flux emergent from the lower boundary on the middle atmosphere is primarily the radiative flux that is independent of the temperature in the middle atmosphere. For example, the effect of the solar radiative flux can often be parameterized by an effective albedo of the surface and lower atmosphere (ω_0), which enhances the heating rate due

to absorption of the Chappuis bands (410-750 nm) by ozone in the stratosphere caused by surface reflection and multiple scattering of clouds, aerosols and air (*e.g*., Meier *et al*. 1982; Nicolet *et al*. 1982). The calculation of the generalized damping matrix **A** for a basic state of temperature and species distributions can be implemented by a radiation algorithm and molecular diffusive formulation. In this paper, the Johns Hopkins University Applied Physics Laboratory (JHU/APL) middle atmosphere radiation algorithm (Zhu 1994, 2004) is adopted for radiative cooling calculations, and a temperature-dependent thermal conductivity of $\lambda = 5.6\times10^{-4}T^{0.69}$ $[\mathrm{kg\cdot m\cdot s^{-3}\cdot K^{-1}}]$ (Banks and Kockarts 1973) is used for calculating the diffusive heat flux of $\lambda\partial T/\partial z$. Each column (vertical axis) of **A** represents the vertical profile of cooling rate and diffusive heating rate difference ($\mathrm{K\,day^{-1}}$) due to a unit change in temperature at altitude *z* (horizontal axis).

In the middle atmosphere, the effect of line overlap is negligible for the infrared radiative cooling rate calculations. As a result, the total infrared cooling rate can be evaluated as the sum of the cooling rates due to CO_2, O_3 and H_2O (Zhu 1994). Therefore, the term $\Delta'\mathbf{R}$ in Eq. (4) or (5) becomes,

$$\Delta'\mathbf{R} = \Delta\mathbf{R}^{\mathrm{CO2}} + \Delta\mathbf{R}^{\mathrm{O3}} + \Delta\mathbf{R}^{\mathrm{H2O}}. \qquad (6)$$

Note that for the middle atmosphere, Eq. (6) is nearly exactly satisfied. In other words, the linear separation of the partial infrared radiative cooling rate due to individual gases in the middle atmosphere is satisfied automatically, which is not the case for the troposphere. Therefore, the only linear approximation introduced to the infrared radiative cooling rate is the separation of the temperature variation, as indicated in Eq. (4). In this sense, fewer approximations for the middle atmosphere feedback analysis have been used than those for the troposphere and surface temperatures, *e.g*., the CFRAM (LC09) and PRP method (Soden *et al*. 2008).

For radiative heating by solar flux, we still need to invoke a linear approximation to decompose the energy perturbation into individual components by different factors, namely,

$$\Delta\mathbf{S} \approx \frac{\partial \mathbf{S}}{\partial [\mathrm{O}_3]}\Delta[\mathrm{O}_3] + \frac{\partial \mathbf{S}}{\partial [\mathrm{O}_2]}\Delta[\mathrm{O}_2] + \frac{\partial \mathbf{S}}{\partial F_{107}}\Delta F_{107} + \frac{\partial \mathbf{S}}{\partial \omega_0}\Delta\omega_0 , \tag{7a}$$

or

$$\Delta\mathbf{S} \approx \Delta\mathbf{S}^{\mathrm{O3}} + \Delta\mathbf{S}^{\mathrm{O2}} + \Delta\mathbf{S}^{\mathrm{F107}} + \Delta\mathbf{S}^{\omega 0} , \tag{7b}$$

where $[\mathrm{O}_3]$ and $[\mathrm{O}_2]$ are the ozone and oxygen densities, respectively. F_{107} is the 10.7-cm solar radio flux (in units of 10^{-22} W m^{-2} Hz^{-1}), which is a parameter representing the solar flux variations, and ω_0 is the effective albedo of surface and the lower atmosphere. The effect of $[\mathrm{O}_2]$ variation on the energy perturbation ($\Delta\mathbf{S}^{\mathrm{O2}}$) is only important in the lower thermosphere. In the middle atmosphere, the vertical velocity associated with the meridional circulation or the residual circulation plays an important role in coupling the radiation with dynamics and photochemistry. Here, invoking a linear approximation, we may explicitly extract this special term of "dynamical response" from the total non-radiative energy source (Holton 2004):

$$\Delta\mathbf{Q} = \mathbf{\Theta}\Delta\mathbf{w}^{*} + (\Delta\mathbf{\Theta})\mathbf{w}^{*} + \Delta''\mathbf{Q}^{eddy} , \tag{8}$$

where the diagonal matrix $\mathbf{\Theta}$ is the static stability parameter and column vector $\Delta\mathbf{w}^{*}$ is the variation in resolved vertical velocity that yields the change in adiabatic cooling. The last term in Eq. (8) represents the contributions due to unresolved small-scale eddies and the energy transport by horizontal wind among neighboring vertical columns. Note that although the non-radiative energy source ($\Delta\mathbf{Q}$) can be evaluated from the dynamical modules during runtime of model integrations as reported in Lu and Cai (2010) and Song *et al*. (2014), it cannot be obtained directly from observations. It can also be evaluated as an energy residual term to balance the net radiative cooling rate and molecular mixing according to Eq. (3): $\Delta\mathbf{Q} = \Delta(\mathbf{R} - \mathbf{Q}_{mol} - \mathbf{S})$. Such an approach of using better-defined thermal forcing to diagnose mechanical forcing was also proposed in Zhu *et al*. (2001) to diagnose the dynamical fields in the middle atmosphere. As reported in Lu and Cai (2010) and Song *et al*. (2014), $\Delta\mathbf{Q}$ inferred explicitly from dynamical fields is almost identical to that inferred as an energy residual term. Given $\Delta\mathbf{Q}$, we then use Eq.

(8) to obtain $\Delta''\mathbf{Q}^{eddy}$ from the difference between $\Delta\mathbf{Q}$ and the other two terms which can be calculated from the available $\mathbf{T}$ and $\mathbf{w}^*$ profiles.

Substituting Eqs. (6)-(8) into Eq. (5), we obtain

$$\Delta\mathbf{T} = \mathbf{Z}\cdot\{-\Delta\mathbf{R}^{\mathrm{CO2}} + (\Delta\mathbf{S}^{\mathrm{O3}} - \Delta\mathbf{R}^{\mathrm{O3}}) + \Delta\mathbf{S}^{\mathrm{F107}} - \Delta\mathbf{R}^{\mathrm{H2O}} + \Delta\mathbf{S}^{\omega 0} + \mathbf{\Theta}\Delta\mathbf{w}^* + (\Delta\mathbf{\Theta})\mathbf{w}^* + \Delta''\mathbf{Q}^{eddy}\}, \quad (9)$$

where $\mathbf{Z} = \mathbf{A}^{-1}$ is the generalized relaxation matrix. Note that the change of $[O_3]$ in the middle atmosphere contributes to both radiative heating and cooling rate variations. This is similar to H_2O and clouds in the troposphere that can both radiatively heat and cool the atmosphere.

As indicated in LC09, Eq. (9) represents the property of additive thermal responses, *i.e.*, the sum of the partial temperature changes ($\Delta\mathbf{T}^{(n)}$) of the MCFRAM due to individual variations of various external forcing such as $\Delta[CO_2]$ or ΔF_{107} and feedback processes such as $\Delta[O_3]$ is the total temperature change ($\Delta\mathbf{T}^{total}$):

$$\Delta\mathbf{T}^{total} = \sum_n \Delta\mathbf{T}^{(n)}, \quad (10)$$

where

$$\Delta\mathbf{T}^{(n)} = \mathbf{Z}\cdot\Delta\mathbf{F}^{(n)}. \quad (11)$$

Here, we define the total temperature change $\Delta\mathbf{T}^{total}$ to be an observed quantity representing the actual difference in the measured temperatures between the two equilibrium states. The energy perturbations $\Delta\mathbf{F}^{(n)}$ in Eq. (11) denote various terms in the brackets on the right-hand side of Eq. (9). Physically, $\Delta\mathbf{T}^{(n)}$ correspond to the partial temperature changes associated with linear atmospheric thermal responses to the energy perturbations $\Delta\mathbf{F}^{(n)}$ caused by individual parameter variations. Those parameter variations can either be derived from observations or from model output. The physical meanings of these partial temperature changes ($\Delta\mathbf{T}^{(n)}$) in MCFRAM are shown in Table 1. The sum of the first six components forms the partial temperature change due to radiative processes $\Delta\mathbf{T}^{rad} = \Delta\mathbf{T}^{(1-6)}$. The non-radiative partial temperature change $\Delta\mathbf{T}^{non-rad}$ includes changes due to both the grid resolved and unresolved atmospheric motions. It should be

noted that $\Delta\mathbf{T}^{rad}$ has been derived from the changes in net radiative heating rate *excluding* the cooling rate change due to the temperature variation itself, *i.e.*, the terms ($\Delta\mathbf{S} - \Delta'\mathbf{R}$) in Eq. (5). One important reason that the temperature variation is singled out in Eq. (4) is that the generalized damping matrix **A** introduced in Eq. (5) is well-behaved and always invertible.

The additive relation (10) for the temperature changes is an alternative expression of the energy Eq. (3) that too is additive. A linear transformation that singles out the total temperature change from energy difference on the left-hand side of Eq. (3) also leads to the partial temperature differences as shown in Eq. (11) and allows us to derive this alternative relationship. The principal advantage of the additive relation (10) for temperature over the additive relation (3) for energy is that $\Delta\mathbf{T}^{total}$ on the left-hand side of Eq. (10) is a directly observed and commonly used quantity, which can serve as a natural and standard scale for comparison.

In addition to temperature **T** and its changes $\Delta\mathbf{T}^{(n)}$, we may also choose a different variable to express the energy budget and its changes. For example, given a vertical profile of "thermal response" as expressed by the temperature changes $\Delta\mathbf{T}^{total}$ and $\Delta\mathbf{T}^{(n)}$, we may calculate the corresponding *local* "dynamical response" of changes in meridional circulation by the following linear transformation

$$\Delta\mathbf{w}^{total} = (\mathbf{\Theta}^{-1}\mathbf{A}) \cdot \Delta\mathbf{T}^{total} \tag{12}$$

and

$$\Delta\mathbf{w}^{(n)} = (\mathbf{\Theta}^{-1}\mathbf{A}) \cdot \Delta\mathbf{T}^{(n)}, \tag{13}$$

where we have already assumed a stable stratification of the atmosphere so that the matrix $\mathbf{\Theta}$ never becomes singular or ill-conditioned (Holton 2004). This condition generally holds well in the middle atmosphere. Substituting Eqs. (12)-(13) into Eq. (10) yields a different form of energy budget equation:

$$\Delta\mathbf{w}^{total} = \sum_n \Delta\mathbf{w}^{(n)}. \tag{14}$$

Again, note that in MCFRAM the total temperature change $\Delta\mathbf{T}^{total}$ is a physical quantity that is directly measurable. On the other hand, the total resolved *local* vertical velocity defined by Eq. (12) is only an equivalent quantity corresponding to the observed $\Delta\mathbf{T}^{total}$. The physically measurable vertical velocity is $\Delta\mathbf{w}^{*}$ and is related to the contribution of an equivalent partial temperature change via $\Delta\mathbf{w}^{*} = (\boldsymbol{\Theta}^{-1}\mathbf{A}) \cdot \Delta\mathbf{T}^{w*}$ (Table 1).

It is noted that the *global* "thermal response" and "dynamical response" are closely related in a more general perspective under the statistical equilibrium condition (Fels 1987; Zhu *et al*. 2001). The meteorological underpinning of such a relation in a meridional plane is the thermal wind balance. Specifically, even though the meridional circulation is driven by the meridional gradient of the diabatic heating, the vertical gradient of the diabatic heating is exactly balanced by the meridional gradient of the mechanical forcing (Fels 1987; Zhu *et al*. 2001). As a result, the strengthening of the meridional circulation such as the Brewer-Dobson circulation in the lower stratosphere can be interpreted either as a response to changes in thermal forcing or as a response to changes in wave drag. Therefore, the spatial structures of $\Delta\mathbf{T}^{(n)}$ derived from MCFRAM based on the energy equation also provide us with a global insight into both the thermal and dynamical responses in the middle atmosphere. Note that MCFRAM as outlined by Eqs. (10)-(11) together with Table 1 generally applies to independent columns of the middle atmosphere. The spatial structure of the derived $\Delta\mathbf{T}^{(n)}$ is only a result of the diagnostic analysis but is not explicitly included in the analysis procedure.

2.2 Eigenmodes of the generalized damping matrix and illustration of MCFRAM

In Eq. (5) or (9), there is a common matrix factor that linearly multiplies all the radiative and non-radiative energy perturbation terms. As a result, both the magnitude and vertical structure of the climate feedbacks are significantly influenced by the generalized damping matrix **A** defined in Eq. (5) or the generalized relaxation matrix **Z** defined in Eq. (9). Table 1 explicitly shows that the partial temperature changes are proportional to the energy perturbation vectors $\Delta\mathbf{F}^{(n)}$ for different processes and are modified by the same generalized relaxation matrix **Z**.

Specifically, for a given vertical profile of the energy perturbation the spatial structure of partial temperature change is completely determined and can be understood by the eigenvectors ($\boldsymbol{\xi}_i$) and eigenvalues (λ_i) of $\mathbf{A}$ or $\mathbf{Z} = \mathbf{A}^{-1}$:

$$\mathbf{A}\boldsymbol{\xi}_i = \lambda_i \boldsymbol{\xi}_i \quad \text{or} \quad \mathbf{Z}\boldsymbol{\xi}_i = \lambda_i^{-1}\boldsymbol{\xi}_i, \quad i=1,2,\ldots,N, \tag{15}$$

where N is the total number of vertical layers. Equation (15) indicates that the eigenvalues of $\mathbf{Z}$ are the inverse of the eigenvalues of $\mathbf{A}$ corresponding to the same eigenvectors. Here, λ_i and λ_i^{-1} can be called generalized damping rate and relaxation time corresponding to the perturbation eigenvector $\boldsymbol{\xi}_i$, respectively. In the absence of molecular viscosity ($\mathbf{Q}_{mol} = 0$) the generalized damping matrix is given by $\mathbf{A} = \partial\mathbf{R}/\partial\mathbf{T}$. Its eigenvalue λ_i happens to be the radiative damping rate of a temperature perturbation (*e.g.*, Goody and Yung 1989, Zhu and Strobel 1991). The effect of the vertical structure of the temperature perturbation characterized by its eigenvector $\boldsymbol{\xi}_i$ on the radiative damping rate has been well documented (Zhu and Strobel 1991, Zhu 1993). The occurrence of the radiative damping rate in MCFRAM is a natural consequence that the basic MCFRAM equation (9) or (10) is an energy perturbation equation. When the energy perturbation is specifically referring to the cooling rate change in association with a temperature perturbation that has been singled out among all the other changes, it is the radiative damping rate that establishes the connection between the two perturbations. In general, the magnitude of λ_i under non-vanishing $\mathbf{Q}_{mol}$ conditions is proportional to the magnitudes of the radiative cooling rate and molecular viscosity. It increases with the increasing characteristic vertical wavenumber of the energy perturbation, *i.e.*, the wavenumber of cooling rate variation or the temperature variation.

The infrared radiative heat exchange by CO_2 and O_3 makes a major contribution whereas cool-to-space cooling by H_2O makes a minor contribution to the radiative cooling rate in the middle atmosphere (Zhu 1994). Here, we use the T and $[O_3]$ observed from the SABER onboard the TIMED satellite to derive $\mathbf{A}$ or $\mathbf{Z}$ and to perform the eigenmode analysis to illustrate the general characteristics of the eigenvector of $\mathbf{A}$ or $\mathbf{Z}$ in the middle atmosphere. The needed global mean H_2O profile for the radiation algorithm is derived from the 3D Goddard Earth Observing

System chemistry-climate model (GEOSCCM; Pawson *et al*., 2008). In Fig. 1, we show the TIMED/SABER measured global mean T and $[O_3]$ averaged over a 54°S-54°N latitudinal range and a 12-year period of 2002-2013. The SABER measurements ranging from 20 km to 110 km in the middle atmosphere are merged with the US Standard Atmosphere in the troposphere. The vertical resolution of all the input profiles from surface to 110 km is about 0.7 km. The radiative heating and cooling rate calculations based on the JHU/APL radiation algorithm are performed in the entire vertical domain of 157 layers whereas the MCFRAM analysis is applied to the top 129 layers (N=129) that corresponds to a middle atmosphere ranging from 10 km to 110 km. The matrix **A** or **Z** has dimensions of 129×129 with 129 eigenmodes. Any given vertical profiles of the energy perturbations ($\Delta\mathbf{F}^{(n)}$) can be decomposed by a complete set of the eigenvectors, with each component decaying, *i.e*., relaxing to 0, at a rate proportional to the inverse of their corresponding eigenvalues. Figures 2 shows a set of 17 selected vertical eigenmodes of the generalized damping matrix **A** calculated from T and $[O_3]$ shown in Fig. 1 based on the JHU/APL radiation algorithm (Zhu 1994, 2004). The CO_2 volume mixing ratio in the calculation is set at a 2005 level of 380 ppmv. The eigenmodes describe a quantitative relationship between the energy perturbations and the corresponding temperature perturbations. The eigenvalues (λ_i) of the selected eigenvectors (ξ_i) range from a maximum value of $\lambda_{\max} = 18.98\ \text{day}^{-1}$ (blue line marked with circles in Fig. 2a) to a minimum value of $\lambda_{\min} = 0.023\ \text{day}^{-1}$ (blue dashed line in Fig. 2d). The vertical eigenmode of the largest damping rate corresponding to the smallest relaxation time ($\lambda_{\max}^{-1} = 0.053\ \text{day}$) is a wave packet located at 107 km with a very small vertical scale of ~4 km. That particular wavy energy perturbation will be effectively smoothed out in a very short period and produces a very small temperature perturbation. On the other hand, the eigenmode with the smallest damping rate has a vertical structure of a near uniform heating or cooling near the tropopause. This mode has the largest relaxation time ($\lambda_{\min}^{-1} = 43.4\ \text{day}$) that will yield the largest response in partial temperature change for a given unit of heating or cooling rate perturbations.

There are two distinct features shown in Fig. 2. First, there exists a strong scale-dependence of the eigenvectors for the generalized damping matrix **A**. Eigenvectors corresponding to large-scale vertical perturbations have small eigenvalues. Second, the magnitude of the eigenvalue decreases as the location of the characteristic perturbation shifts from the upper middle atmosphere to the lower middle atmosphere. As a result, we note that when the value of eigenvalue decreases as we move consecutively from panel (a) to panel (d) the vertical scale of eigenvector increases and the location of its main perturbation shifts to the lower altitude. This is consistent with the general nature of the radiative damping of temperature perturbation in the middle atmosphere (*e.g.*, Goody and Yung 1989; Zhu 1993). In addition, the effect of the molecular diffusion included in **A** has the same general characteristics of small-scale perturbations at a higher altitude being more effectively damped or filtered. To show the general nature of scale-dependence and its departure from a precise one for the eigenmodes in the entire middle atmosphere we perform a Fourier transform to all 129 eigenvectors and calculate their power spectral densities (PSDs) (Zhu and Strobel 1991; Zhu 1991). Figure 3 shows a scatter plot between the generalized damping rate λ_i and the wavenumber of the maximum peak in the PSD for all 129 eigenvectors. Also shown in the figure are the analytic expression for the parameterized radiative damping rate proposed in Zhu (1993) and a square fit ($\lambda_i \sim m^2$) to the diffusive damping. Because of the vertical inhomogeneity of the atmosphere, the relationship is not single-valued. For example, a wave packet with a large vertical scale located in the mesopause could have the same damping rate as one in the stratosphere with a small vertical scale. A better parameterization for radiative damping in practice is to introduce a scale-dependent radiative damping rate that also varies with altitude (Fels 1982; Zhu 1993).

The effect of the vertical structure of the energy perturbations on the partial temperature changes through **A** or **Z** can be seen from Fig. 4 where the partial temperature changes of $\Delta\mathbf{T}^{CO2}$, $\Delta\mathbf{T}^{O3}$ and $\Delta\mathbf{T}^{F107}$ are calculated from Table 1 based on three energy perturbations caused by changing three atmospheric parameters (i) CO_2 volume mixing ratio is doubled from 380 ppmv

to 760 ppmv, (ii) O_3 volume mixing ratio is uniformly reduced by 50%, and (iii) solar index $F_{10.7}$ is increased from 60 to 260 (in units of 10^{-22} W m^{-2}Hz^{-1}). The vertical structure of temperature difference (Fig. 4b) is smoother than and significantly different from that of the heating rate variations (Fig. 4a). This is mainly due to the scale-dependence of the generalized damping rate (λ_i) where smaller scale energy perturbations are more effectively damped, *i.e.*, partial temperature changes are smoother than energy perturbations. Furthermore, the lower middle atmosphere is more sensitive in partial temperature changes to a smaller energy perturbation due to greater opacity than the upper middle atmosphere.

3. Application of MCFRAM to TIMED/SABER measurements

Application of MCFRAM is straightforward once the input fields of various parameter variations as indicated in Eqs. (5) and (9) together with Table 1 are available. While climate models (such as the GEOSCCM) can provide all the needed and uniformly distributed global input fields, satellite measurements often provide only part of the needed fields to derive the balanced additive relation (10). In this section, we show the MCFRAM analyzed results by using SABER measured T and O_3 fields (Russell *et al*. 1999). We use the V1.07 SABER data available to the public from the TIMED mission data center (http://www.timed.jhuapl.edu) which yields significantly improved temperature retrievals at high latitude summer (Kutepov *et al*. 2006).

Figures 5a and 5b show the zonal mean T and O_3 fields in the middle atmosphere derived from SABER measurements in the low and mid-latitudes averaged over a 12-year period of 2002-2013. Shown in Figs. 5c and 5d are the T and O_3 difference between two time-mean states covering the periods of 2002-2003 and 2008-2009, respectively. Though the overall temperature in the middle atmosphere exhibits a noticeable decrease from the 2002-2003 period of near solar maximum to the 2008-2009 period of solar minimum over most regions, there are some regions showing positive temperature anomalies in response to the solar energy input decrease. We note that the observed temperature difference represents the total effects contributed by various

processes including the solar flux changes due to solar cycle and man-made variations in CO_2 concentration and other chemical species.

We now apply MCFRAM to the SABER observed *T* and O_3 difference between two periods of 2002-2003 and 2008-2009. The corresponding mean CO_2 mixing ratios and solar flux indices used in MCFRAM analysis for these two periods are [r_{CO2}~374.7 ppmv, F_{107}~167.1] and [r_{CO2}~386.3 ppmv, F_{107}~68.1], respectively. There are 12 yaw cycles in each two-year period with each yaw cycle covering about 60 days. The corresponding local time and latitudinal coverage in two yaw cycles separated by six years are nearly identical. The temperature difference shown in Fig. 5c represents the total temperature difference $\Delta\mathbf{T}^{total}$ as defined in Eq. (10). The MCFRAM analysis is performed separately to the corresponding yaw cycles with the seasonal parameters such as the solar declination angle and $F_{10.7}$ varying with different yaw cycles. The partial temperature changes as defined in Eq. (11) or Table 1 will be the 12-yaw cycle mean of all partial temperature changes between the two yaw cycles in the corresponding time periods separated by 6 years. Given the observed *T*, O_3 and $F_{10.7}$ variations and using the JHU/APL middle atmosphere radiation algorithm, the first three components of the partial temperature changes shown in Table 1, *i.e.*, $\Delta\mathbf{T}^{CO2}$, $\Delta\mathbf{T}^{O3}$ and $\Delta\mathbf{T}^{F107}$, can be explicitly evaluated. Since H_2O and other radiatively active species only make minor contributions to the radiative heating and cooling rate in the middle atmosphere, we expect the sum of the above three terms is approximately the partial temperature change due to radiative transfer $\Delta\mathbf{T}^{rad}$ as described in Table 1. As mentioned before, we use the energy residual of Eq. (3) to estimate $\Delta\mathbf{Q}$ to calculate $\Delta\mathbf{T}^{non-rad}$. In Fig. 6, we show the latitude-altitude distributions of $\Delta\mathbf{T}^{CO2}$, $\Delta\mathbf{T}^{O3}$, $\Delta\mathbf{T}^{F107}$ and $\Delta\mathbf{T}^{non-rad}$. Also shown in the figure are $\Delta\mathbf{w}^{CO2}$ defined by Eq. (13) and the error in $\Delta\mathbf{T}^{non-rad}$ due to linearization, *i.e.*, the difference between $\Delta\mathbf{T}^{non-rad}$ based on the energy residual (Table 1) and the one based on a temperature residual $\Delta\mathbf{T}^{total} - (\Delta\mathbf{T}^{CO2} + \Delta\mathbf{T}^{O3} + \Delta\mathbf{T}^{F107})$.

We note that the middle atmosphere cooling rate by the CO_2 15-μm band is mainly contributed from its cool-to-space component with its escape probability slowly varying with

altitude in the middle atmosphere (Zhu *et al*. 1992). A uniform change in CO_2 mixing ratio also leads to a near uniform change in escape probability in the middle atmosphere. Hence, the maximum response to a uniform increase in CO_2 mixing ratio in the middle atmosphere occurs at the equatorial stratopause (Fig. 6a), where the peak temperature as shown in Fig. 5a produces the largest cooling rate variation. On the other hand, the response $\Delta\mathbf{T}^{O3}$ due to change in O_3 concentration represents a combined effect of both the solar flux heating and O_3 9.6 μm band infrared cooling. Since there are both positive and negative ozone variations between 2002-2003 and 2008-2009 periods (Fig. 5d), the induced partial temperature change $\Delta\mathbf{T}^{O3}$ also shows a non-uniform spatial pattern (Fig. 6b). The peak variation in temperature in the upper mesosphere is mainly due to the change in localized absorption of solar ultraviolet (UV) flux heating whereas the peak variations in the stratosphere are mainly due to the enhanced O_3 9.6 μm band cool-to-space cooling rate variations in a more transparent atmosphere. Here, we note that the middle atmosphere climate responses to the cooling rate changes induced by CO_2 and O_3 variations are different. $\Delta\mathbf{T}^{CO2}$ due to CO_2 variation (Fig. 6a) mostly follows the total temperature field due to a strong dependence of outgoing infrared radiation on the Planck blackbody emission whereas $\Delta\mathbf{T}^{O3}$ due to O_3 variation (Fig. 6b) mostly follows O_3 concentration due to a stronger dependence of radiative emission on more rapidly varying escape probability (Zhu *et al*. 1991). $\Delta\mathbf{T}^{F107}$ shown in Fig. 6c exhibits a pattern of overall monotonic increase in magnitude with altitude mainly due to the fact that solar UV fluxes of greater variations at shorter wavelengths are generally absorbed at higher altitudes.

We note that the overall spatial pattern and magnitude of $\Delta\mathbf{T}^{non-rad}$ shown in Fig. 6d is similar to $\Delta\mathbf{T}^{total}$ shown in Fig. 5c, indicating the importance of dynamical drive of the zonal mean middle atmospheric thermal structure. One striking feature in Fig. 6d is that $\Delta\mathbf{T}^{non-rad}$ is significantly greater and has richer spatial structure than any individual partial temperature change due to radiation processes. In other words, most part of temperature changes in the middle atmosphere are associated with dynamic processes and the corresponding changes in

thermal radiation in turn balance the non-radiative energy source. One plausible explanation is that the middle atmosphere thermal radiative forcing as a whole is largely modulated by the dynamical wave drag, which is strong due to decreasing air density with altitude and significantly inhomogeneous due to randomness of various wave generation and dissipation mechanisms. Furthermore, from a global perspective, the adiabatic heating and mechanical forcing are balanced in a zonally averaged meridional plane under the quasi-equilibrium conditions (Zhu *et al*. 2001). For example, in the lower stratosphere, because the tropopause is much higher (~17 km) in the tropics than in the extratropics (~10 km), an induced thermal cooling in the high-latitude lower stratosphere associated with $\Delta\mathbf{T}^{CO2}$ coupled with a mid-tropospheric warming in the tropics would enhance a meridional gradient of diabatic heating. Such a change in thermal forcing is accompanied by an enhancement in the vertical gradient of the wave drag, which is often considered as a dynamical mechanism of driving the strengthening of the Brewer-Dobson circulation in the lower stratosphere (Butchart *et al*. 2006; Garcia and Randel 2008; Shepherd and McLandress 2011).

The equivalent partial change in vertical velocity due to change in CO_2 as shown in Fig. 6e shows a clear negative correlation to $\Delta\mathbf{T}^{CO2}$ shown in Fig. 6a, indicating the fact that a decrease in atmospheric temperature can be dynamically associated with an increase in adiabatic cooling induced by a strengthening in upward motion. A magnitude of 1K in temperature decrease due to climate forcing is equivalent to an increase of about $0.025\ \mathrm{km\ day^{-1}}$ in vertical velocity in terms of atmospheric dynamical response. Comparison between Fig. 6d and 6f suggests that the linearization from an energy residual to a temperature residual leads to errors of less than 10% in partial temperature changes. This can also be considered as a measure of errors in converting the generic additive relation (3) for energy differences to the MCFRAM additive relation (10) for temperature changes.

Though $\Delta\mathbf{T}^{non-rad}$ could be very large locally, its global average in the middle atmosphere should be much smaller than its typical local values. This is mainly due to the fact that the

globally averaged vertical velocity at a given pressure level should nearly vanish (Olaguer *et al*. 1992), and the main role of propagating waves is to redistribute rather than generate the momentum and heat (*e.g*., Zhu *et al*. 2008, 2010). It is only the eddy diffusion generated by wave breaking and molecular viscosity that will be able to produce a globally averaged heating or cooling rate difference. In Fig. 7a, we plot the globally averaged partial temperature changes as shown in Fig. 6a-d together with the sum of the three components, which gives a very good approximation of $\Delta\mathbf{T}^{rad}$ in the middle atmosphere. The figure shows that $\Delta\mathbf{T}^{rad}$ gradually increases from 0 near 22 km to 1K near 30 km. It remains to be ~1K in the region of 30-70 km. The difference between $\Delta\mathbf{T}^{total}$ derived from the direct measurements by SABER and $\Delta\mathbf{T}^{rad}$ is $\Delta\mathbf{T}^{non-rad}$. Its global mean is shown in Fig. 7b. Figure 7b confirms our conjecture that the globally averaged $\Delta\mathbf{T}^{non-rad}$ is a small difference between globally averaged $\Delta\mathbf{T}^{total}$ and $\Delta\mathbf{T}^{rad}$ in most of the middle atmosphere although locally $\Delta\mathbf{T}^{non-rad}$ is noticeably greater than either $\Delta\mathbf{T}^{total}$ or $\Delta\mathbf{T}^{rad}$. Physically, Fig. 7b also means that the globally averaged climate change in the middle atmosphere is thermally driven below ~70 km where the vertical eddy transport due to wave breaking is expected to be small. An increase in CO_2 concentration coupled with a decrease in solar radiation reduces the net radiative heating rate, which cools the global atmosphere. It should be pointed out that this is not an obvious scenario among several alternatives. For example, an atmosphere can be adiabatically cooled globally at a certain altitude range by a systematic upward motion driven by a radiative heating (*e.g*., Zhu *et al*. 2014). Near and above the mesopause region, globally averaged $\Delta\mathbf{T}^{non-rad}$ is no longer small but of the same order of magnitude as $\Delta\mathbf{T}^{total}$ or $\Delta\mathbf{T}^{rad}$. This is mainly because the gravity wave breaking in the upper mesosphere induces eddy diffusion that irreversibly transports and distributes tracers including the potential temperature associated with atmospheric energy.

It is worth pointing out that the results shown in Fig. 7 independently verify the SABER measurements of T and O_3 and the accuracy of the JHU/APL radiation algorithm for the middle atmosphere. One common way of verifying measurements and testing radiation algorithms is to

evaluate the global radiative balance (Kiehl and Solomon 1986; Olaguer *et al*. 1992). A good radiation algorithm requires the globally averaged net radiative heating rate to be much smaller than the typical values of the localized net radiative heating rate. A more stringent requirement for a good algorithm is to further have a greater sensitivity of heating or cooling rate with respect to variations in radiation parameters while still preserving the property of its globally averaged net radiative heating rate close to zero. Note that $\Delta\mathbf{T}^{rad}$ and $\Delta\mathbf{T}^{non-rad}$ are closely related to the *difference* of the net radiative heating rate and the vertical velocity between two slightly different equilibrium states, respectively. The result shown in Fig. 7a suggests that the JHU/APL radiation algorithm is sensitive to variations in CO_2, O_3 and $F_{10.7}$ and yet the globally averaged $\Delta\mathbf{T}^{non-rad}$ shown in Fig. 7b remains small, as expected for thermally driven global change, based on the premise that the SABER measured T and O_3 fields are accurate as well.

4. Application of MCFRAM to GEOSCCM output fields

Similar to the SABER measurements, we apply the MCFRAM analysis to two-dimensional zonal mean fields derived from the GEOSCCM. The 3D GEOSCCM uses the GEOS-5 atmospheric general circulation model (Rienecker *et al*. 2008) in its forecast-model component, coupled with the stratospheric chemical solver developed as a part of the GSFC 3D chemical-transport model (Douglass *et al*. 1996; Pawson *et al*. 2008). With respect to Rienecker et al. (2008) this version of GEOSCCM also includes a treatment of stratospheric aerosol (Aquila *et al.* 2012; 2013) and a mechanism to generate the QBO using a gravity wave drag parameterization (Molod *et al*. 2012). The GEOSCCM traditionally uses a fixed input solar spectrum, representative of mean solar cycle conditions, and has in fact been used as a no-solar cycle reference model in past CCM intercomparisons (Austin *et al*., 2008). For use in MCFRAM the GEOSCCM has been modified to include a solar cycle through the development of new atmospheric heating and photolysis code (Swartz *et al*. 2012).

In general, the saved fields of GEOSCCM or any other CCMs are not specifically designed for directly performing a full MCFRAM analysis. Additional processing to some of the

output fields is needed in order to produce a set of appropriate input fields for MCFRAM analysis. One potentially important input parameter as shown in Eq. (7) or (9) is the effective albedo of surface and the lower atmosphere (ω_0) that radiatively couples the middle atmosphere with the troposphere and surface. ω_0 is not saved in GEOSCCM as an output field in the simulations used. We therefore use the saved field "TOA net downward shortwave flux" F_{RSR} ($\mathrm{W\ m^{-2}}$) to derive ω_0. F_{RSR} is related to ω_0 by the following relationship

$$F_{RSR} = S_{TOA}(1-\omega_0) = S_0\mu(1-\omega_0), \tag{16}$$

where S_{TOA} is the TOA downward solar flux with S_0 and μ being the solar constant (= 1366 $\mathrm{W\ m^{-2}}$, Liou 2002) and cosine of the solar zenith angle, respectively. For a given zonal mean F_{RSR}, the diurnally averaged S_{TOA} can be calculated by (Cogley and Borucki 1976, Zhu 1994)

$$\overline{S}_{TOA} \equiv S_0\overline{\mu} = \frac{S_0}{\pi}\int_{\max(0,A-B)}^{\max(0,A+B)} \frac{\mu d\mu}{\sqrt{B^2-(\mu-A)^2}}, \tag{17}$$

where $A = \sin\phi\sin\delta$, $B = \cos\phi\cos\delta$, ϕ is the latitude, and δ is the solar declination angle. We finally get the ω_0 for applying MCFRAM to a zonal mean field

$$\omega_0 = 1 - \frac{\overline{F}_{RSR}}{\overline{S}_{TOA}}. \tag{18}$$

Note that when $A+B \le 0$ the sun does not rise and $\overline{S}_{TOA} = 0$ and ω_0 can be any value. Under such a circumstance, we set the variation of ω_0 between the two states 1 and 2 to be zero. When $A-B>0$ then the sun does not set and the lower limit of the integration in Eq. (17) is set to $A-B$. Since the upper boundary of the current GEOSCCM is below the mesopause, where the effect of O_2 variation is negligible in energy budget, we will neglect $\Delta\mathbf{T}^{O2}$ in this paper.

Another issue in implementing MCFRAM analysis based on model output fields is that most CCMs such as the GEOSCCM only save separately the total solar heating and infrared cooling rates but not the individual components contributed by different absorbers and solar flux variations. We have already pointed out previously through Eq. (6) that the separation of cooling

rate components in the middle atmosphere is very simple because the effect of line overlapping is negligible. On the other hand, Eq. (7) suggests that it requires a significant overhaul to the online radiation code in any CCMs in order to derive and save heating rate contributions by different components mainly because of the nonlinear effect between solar flux and absorber. One way to get around the whole issue is to calculate all the radiative heating and cooling perturbation terms offline and introduce two error terms to the basic MCFRAM Eqs. (10) and (11) (Taylor *et al*. 2013; Sejas *et al*. 2014):

$$\Delta\mathbf{T}^{total} = \sum_{n} \Delta\mathbf{T}^{(n)} - \Delta\mathbf{T}^{err1} - \Delta\mathbf{T}^{err2}. \tag{19}$$

Here, the two partial temperature changes due to radiation errors are calculated based on GEOSCCM-saved total solar heating and infrared cooling rates together with the offline radiation algorithm:

$$\Delta\mathbf{T}^{err1} = \mathbf{Z}\cdot\Delta\mathbf{S}^{err} \quad \text{and} \quad \Delta\mathbf{T}^{err2} = \mathbf{Z}\cdot(-\Delta\mathbf{R}^{err}), \tag{20a,b}$$

where $\Delta\mathbf{S}^{err}$ and $\Delta\mathbf{R}^{err}$ are respectively the changes in total radiative heating and cooling rates between two states 1 and 2 derived from the offline and GEOSCCM online radiation algorithms

$$\Delta\mathbf{S}^{err} = \Delta\mathbf{S}^{off} - \Delta\mathbf{S}^{ccm} \quad \text{and} \quad \Delta\mathbf{R}^{err} = \Delta\mathbf{R}^{off} - \Delta\mathbf{R}^{ccm}. \tag{21a,b}$$

It has been suggested that the error terms are mostly contributed from the different averaging procedures between the online and offline calculations (Taylor *et al*. 2013; Sejas *et al*. 2014). Additional errors will also contribute to partial temperature changes due to radiation errors when different radiation algorithms are adopted for the online and offline radiative heating and cooling rate calculations. The error introduced by inferring $\Delta\mathbf{Q}$ from radiative forcing evaluated from the offline radiative transfer model calculations can be estimated and analyzed by a comparison with that derived directly from CCM outputs saved during runtime (Sejas *et al*. 2014).

In this paper, we choose the same output time periods of 2002-2003 (near solar maximum) and 2008-2009 (solar minimum) from one GEOSCCM simulation as those for

SABER measurements used in the last section to perform the MCFRAM analysis. In Fig. 8, we show the variation in effective albedo of the surface and lower atmosphere scaled by the diurnally averaged solar radiation $(S_0\bar{\mu})\Delta\omega_0$ as a function of month and latitude over the 24-month period. The figure shows a typical variation of ~5 W m^{-2} that is about 1% of the globally averaged solar flux ($S_0/4$) and is one order of magnitude greater than the variation in solar constant for the 11-year solar cycle (Lean 1991). The figure shows significant geographic and transient variations with peak values appearing near equatorial and summer polar areas where the maximum mean solar fluxes are deposited. Climate change or the system's feedback response is often associated with a radiative forcing scaled by the changes in the total radiation flux. Since the energy deposition in the atmosphere at different wavelengths varies drastically with spatial and temporal distributions of absorbers, the change in the input solar energy may not be able to fully represent how the system responds. On the other hand, the MCFRAM analysis based on Eqs. (10)-(11) together with Table 1 provides us with a complete view of the system response in the same variable and units under an observational constraint of the measured total temperature change ($\Delta\mathbf{T}^{total}$).

In Fig. 9, we show all the partial temperature change components in Table 1 in the middle atmosphere below 70 km that can be directly calculated based on GEOSCCM output fields and the offline JHU/APL radiation algorithm. Panels (a)-(j) correspond to the first 10 rows in Table 1 plus Eqs. (20a, b) but excluding $\Delta\mathbf{T}^{O2}$, which is negligible below the mesopause. Panels (k) and (l) are respectively the partial temperature changes due to all radiative processes ($\Delta\mathbf{T}^{rad}$) with the offline radiation algorithm only ($\Delta\mathbf{T}^{rad}_{offline}$) and that including the online correction terms ($\Delta\mathbf{T}^{rad}_{online}$), *i.e.*

$$\Delta\mathbf{T}^{rad}_{online} = \Delta\mathbf{T}^{rad}_{offline} - \Delta\mathbf{T}^{err1} - \Delta\mathbf{T}^{err2}. \quad (22)$$

Panel (m) sums all the $\Delta\mathbf{T}^{(n)}$ components that can be directly calculated

$$\Delta\mathbf{T}^{sum}_{online} = \Delta\mathbf{T}^{rad}_{online} + \Delta\mathbf{T}^{w^*} + \Delta\mathbf{T}^{\Theta}. \quad (23)$$

608 Panels (n) and (o) are the residual partial temperature changes corresponding to the online
609 versions of $\Delta\mathbf{T}^{eddy}$ and $\Delta\mathbf{T}^{non-rad}$ defined in Table 1, respectively.

610 We first note that the overall patterns and magnitudes of the partial temperature changes
611 $\Delta\mathbf{T}^{CO2}$ and $\Delta\mathbf{T}^{F107}$ (Figs. 9a and 9c) that are primarily induced by the variations of the external
612 forcing are nearly identical to those derived by SABER measurements in the common domain
613 (Figs. 6a and 6c). However, GEOSCCM shows an additional strengthening in partial temperature
614 change associated with the CO_2 cooling in the available high latitude and polar regions,
615 especially in the southern hemisphere mesosphere where the coldest temperature often occurs
616 near the summer mesopause (Lubken 1999; Lubken *et al*. 1999). This is caused by a non-
617 localized heat exchange between the warmer stratopause and colder mesopause when the CO_2 15
618 μm band transmission behaves transparently and the summer mesopause receives net radiative
619 heating from the stratopause (Zhu *et al*. 1992). An increase in CO_2 concentration increases the
620 atmospheric opacity that leads to a reduction in summer mesopause net heating rate.
621 Furthermore, there exists a local maximum in CO_2 15 μm cooling rate near the winter polar
622 mesopause due to the combination of local thermodynamic equilibrium conditions, a near
623 uniform temperature, and a near transparent emission to space (Zhu 1994). This too contributes
624 to the strengthening in $\Delta\mathbf{T}^{CO2}$ in the high-latitude and polar mesosphere regions. There exists a
625 significant difference in $\Delta\mathbf{T}^{O3}$ between GEOSCCM fields (Fig. 9b) and SABER measurements
626 (Fig. 6b). This is not surprising because the middle atmosphere O_3 and its variability are very
627 sensitive to a strong nonlinear coupling between photochemistry and dynamics. For example, the
628 largely off-set peaks in $\Delta\mathbf{T}^{O3}$ in the equatorial lower stratosphere may well reflect the degree of
629 fidelity of GEOSCCM simulation to the equatorial quasi-biennial oscillation phenomenon.

630 The partial temperature change $\Delta\mathbf{T}^{H2O}$ as shown in Fig. 9d makes a much smaller
631 contribution and is negative in the low latitude but positive in part of the midlatitude in the
632 middle atmosphere. Middle atmosphere H_2O may increase with time as a result of increasing
633 CH_4 in the troposphere (Zhu *et al*. 1999). Its decadal change could also be well correlated to the

equatorial sea surface temperature that largely determines the coldness of tropopause to limit the direct entry of H_2O into the stratosphere (Solomon *et al*. 2010). The existence of large regions of both positive and negative $\Delta\mathbf{T}^{H2O}$ in the middle atmosphere is an indication that both processes play important roles in determining H_2O concentration in the time period of 2002-2009. The contribution by the lower atmosphere effective albedo $\Delta\mathbf{T}^{\omega 0}$ is even smaller than $\Delta\mathbf{T}^{H2O}$ by nearly one order of magnitude and changes are largely confined in the stratosphere (Fig. 9e). Comparison between Fig. 8 and Figs. 9a-e gives us one example that the MCFRAM with its key additive property provides us with a more direct and quantitative insight into the relative importance of different factors of climate forcing and feedback processes when they are constrained under the same scale with the same units. Panels (f) and (g) represent the part of the dynamical effects on the atmospheric thermal response that can be easily evaluated based on the available model output fields. As we have already conjectured in discussing the MCFRAM applications to the SABER measurements, the directly calculable components of $\Delta\mathbf{T}^{non-rad}$ are overwhelmingly large with the majority of the contributions coming from $\Delta\mathbf{T}^{w^*}$. We note that the peak values of $\Delta\mathbf{T}^{w^*}$ occur near polar areas and arctic and antarctic circles, where the spherical geometry may lead to unusually large variability in solar heating rate or flow divergence, both in the real atmosphere and in numerical models.

Panels (h) and (i) in Fig. 9 show the partial temperature changes, $\Delta\mathbf{T}^{err1}$ and $\Delta\mathbf{T}^{err2}$, due to differences in heating and cooling rates between the offline and online calculations, respectively. The figures show that the differences are small in most regions of the middle atmosphere except $\Delta\mathbf{T}^{err1}$ near the low latitude upper boundary and $\Delta\mathbf{T}^{err2}$ near the polar area. We note that the heating rate difference associated with $\Delta\mathbf{T}^{err1}$ by the solar radiation near model's upper boundary is sensitive to the shielding effect of the solar flux by the absorber column above the upper boundary. Furthermore, the sensitivity decreases with increasing latitude as the slant path also increases. The high latitude cooling rate difference associated with $\Delta\mathbf{T}^{err2}$ is likely sensitive to the non-localized heat exchange when the vertical temperature gradient is

660 large. Specifically, the heat exchange by the CO_2 15-μm band becomes transparent above the
661 stratopause for a uniform CO_2 mixing ratio distribution whereas the O_3 9.6 μm band emission
662 could be transparent in the entire atmosphere in regions where the O_3 concentration is low (Zhu
663 *et al*. 1991, 1992, Zhu 1994). The issue of $\Delta\mathbf{T}^{err1}$ and $\Delta\mathbf{T}^{err2}$ will be further pursued in the next
664 stage of investigation.

665 Figure 9j shows the measurable temperature difference ($\Delta\mathbf{T}^{total}$) between the two
666 equilibrium states 1 and 2, which is the difference of the model output temperature fields.
667 Comparing with Fig. 5c, we note that both the modeled and SABER measured $\Delta\mathbf{T}^{total}$ show
668 positive-negative paired peaks of the same magnitudes near 50° latitudes and equatorial lower
669 stratosphere. We note that $\Delta\mathbf{T}^{total}$ provides an observational constraint and a unified or a
670 standard scale to all the other sensitivity responses in the MCFRAM analysis. Recall that
671 MCFRAM (or CFRAM) was developed from the energy budget equation (1) or (2). In addition
672 to changes in the energy budget due to all the parameter variations shown in panels (a)-(g), the
673 most prominent and well behaved one is the change in cooling rate and the diffusive heat
674 exchange caused by the variation of atmospheric temperature **T**. The well-behaved nature of
675 $\Delta(\mathbf{R}-\mathbf{Q}_{mol})$ with respect to **T** in Eq. (4) makes the generalized damping matrix **A** always
676 invertible. Furthermore, the temperature **T** is a directly measurable and most common variable.
677 These two features can be considered the underpinning for MCFRAM that exclusively separates
678 the temperature component of variation in the energy budget from all the other components in
679 Eq. (4) and set it to be a standard scale to be compared to all the other feedback responses.
680 Panels (k) and (l) in Fig. 9 show the partial temperature changes due to radiative processes based
681 on offline and online radiation algorithms, $\Delta\mathbf{T}^{rad}_{offline}$ and $\Delta\mathbf{T}^{rad}_{online}$ ($=\Delta\mathbf{T}^{rad}_{offline}-\Delta\mathbf{T}^{err1}-\Delta\mathbf{T}^{err2}$),
682 respectively. We note that the magnitude of $\Delta\mathbf{T}^{rad}$ increases with altitude, which is consistent
683 with that of the measurable $\Delta\mathbf{T}^{total}$. However, there exist significant differences in spatial
684 structure contributed from the partial temperature changes due to non-radiative processes
685 $\Delta\mathbf{T}^{non-rad}$. Since $\Delta\mathbf{T}^{non-rad}$ is dependent on atmospheric motion that is strongly nonlinear and

686 contains many different scales, we expect the magnitude $\Delta\mathbf{T}^{non-rad}$ to be reduced when an
687 ensemble average is taken for the MCFRAM analysis to the output fields from many different
688 runs of GEOSCCM in our future investigations.

689 Among all the components $\Delta\mathbf{T}^{(n)}$ listed in Table 1 the biggest component that can be
690 directly calculated as shown in Fig. 9f is $\Delta\mathbf{T}^{w^*}$. Its typical localized value is nearly an order of
691 magnitude greater than temperature changes $\Delta\mathbf{T}^{total}$ or $\Delta\mathbf{T}^{rad}$ as shown in Fig. 9j-9l. As a result,
692 if we sum up all the terms in Table 1 that can be directly calculated, $\Delta\mathbf{T}^{(1-8)}$ as shown in Fig. 9m
693 in its online version, then its overall spatial distribution will be dominated by that of $\Delta\mathbf{T}^{w^*}$. The
694 last two panels (n) and (o) in Fig. 9 correspond to two last partial temperature changes in Table
695 1, $\Delta\mathbf{T}^{eddy}$ and $\Delta\mathbf{T}^{non-rad}$, calculated by the residual method. $\Delta\mathbf{T}^{eddy}$ is due to dynamical heating
696 contributed by the unresolved eddies and horizontal winds. $\Delta\mathbf{T}^{non-rad}$ is $\Delta\mathbf{T}^{eddy}$ plus the partial
697 temperature changes associated with the adiabatic cooling due to vertical motion that can be
698 calculated based on the column profiles. We see again that $\Delta\mathbf{T}^{eddy}$ largely cancels $\Delta\mathbf{T}^{w^*}$
699 contained in $\Delta\mathbf{T}^{(1-8)}$ mostly due to the energy perturbation associated with the horizontal
700 motions. Since the localized partial temperature changes due to radiative processes $\Delta\mathbf{T}^{rad}$ shown
701 in panel (l) is smaller than the local values of $\Delta\mathbf{T}^{total}$ shown in panel (j), the overall magnitude
702 and spatial structure of $\Delta\mathbf{T}^{non-rad}$ as shown in the last panel (o) is similar to those of $\Delta\mathbf{T}^{total}$,
703 indicating dynamical processes dominate the local structure of the total partial temperature
704 change. This is also consistent with our previous analysis to SABER measurements where Fig.
705 5c and Fig. 6d show large similarities in their overall magnitude and spatial structure.

706 In Fig. 10, we show the globally averaged partial temperature changes presented in Fig.
707 9. Several major features are consistent with those derived from the SABER measurements as
708 shown in Fig. 7: (i) $\Delta\mathbf{T}^{F107}$ makes the largest contribution above ~40 km, (ii) $\Delta\mathbf{T}^{CO2}$ is negative
709 at all altitudes whereas $\Delta\mathbf{T}^{O3}$ is positive in some part of the altitude range, (iii) the globally
710 averaged $\Delta\mathbf{T}^{w^*}$ due to atmospheric circulation makes a small contribution to the global mean
711 climate change in the middle atmosphere below 70 km, which is primarily driven by radiative

processes. In addition to $\Delta\mathbf{T}^{w*}$, the three more terms $\Delta\mathbf{T}^{H2O}$, $\Delta\mathbf{T}^{\Theta}$ and $\Delta\mathbf{T}^{\omega 0}$ have been directly calculated based on the GEOSCCM output fields. Since the globally averaged values of these terms are all smaller than $\Delta\mathbf{T}^{rad}$, our major results derived from the SABER measured **T** and O_3 fields remain valid. We have already mentioned that it is generally unavoidable to adopt an offline radiation algorithm to perform the MCFRAM analysis. We note that $\Delta\mathbf{T}^{err2}$ due to cooling rate difference is negligibly small, and $\Delta\mathbf{T}^{err1}$ increases rapidly near the model's upper boundary, which in turn leads to a large deviation of $\Delta\mathbf{T}^{rad}$ from $\Delta\mathbf{T}^{total}$ near the upper boundary. We note that all the model fields in GEOSCCM, including the atmospheric temperature, have been integrated subject to the influence of a set of prescribed boundary conditions. On the other hand, the magnitude of $\Delta\mathbf{T}^{rad}$ derived from the SABER measurements as shown in Fig. 7 does not systematically increase with the altitude below 80 km, indicating the effect of boundary condition on the heating rate calculations for GEOSCCM fields. We will pursue this issue in our follow-up investigations.

5. Summary

In this study, we have extended the Climate Feedback-Response Analysis Method (CFRAM) for the coupled atmosphere-surface system to the middle atmosphere. The Middle atmosphere CFRAM (MCFRAM) is built upon the atmospheric energy equation per unit mass with radiative heating and cooling rates as its major thermal energy sources. In addition, molecular thermal conduction is added to the energy equation when the upper boundary is extended beyond the mesopause. MCFRAM preserves the unique feature of an additive property for the original CFRAM in which the sum of all partial temperature changes equals the observed temperature change. By introducing the generalized damping (**A**) and relaxation (**Z**) matrices to the basic MCFRAM equation, the relationship between the fundamental quantity of the partial temperature change ($\Delta\mathbf{T}^{(n)}$) and its physical cause of energy perturbation ($\Delta\mathbf{F}^{(n)}$) is quantitatively clarified by the well-documented theory of radiative damping of thermal disturbance in the middle atmosphere. Specifically, we show that **A** serves as a filter that

738 smoothes the small-scale structure in $\Delta\mathbf{F}^{(n)}$. In addition, it is shown that for a given energy
739 perturbation the maximum response in temperature change occurs when the energy perturbation
740 is located at the place where the cooling rate of the mean state reaches it minimum value.

741 The newly developed MCFRAM is applied to two sets of two-dimensional data. One is
742 the zonal mean *T* and O_3 fields in the middle atmosphere derived from SABER measurements in
743 the low and midlatitudes averaged over yaw cycles. The other is the zonal mean fields saved
744 from GEOSCCM simulations. It is found that the spatial structure of the temperature responses
745 to variations of CO_2, O_3 and solar flux are different. $\Delta\mathbf{T}^{CO2}$ closely follows temperature
746 distribution in most of the middle atmosphere because the cool-to-space approximation is valid
747 for an atmosphere with uniformly distributed CO_2 mixing ratio. Both the solar radiation heating
748 and 9.6-μm band cooling by O_3 affect $\Delta\mathbf{T}^{O3}$ in about the same order of magnitude, both
749 processes strongly influenced by O_3 distribution. $\Delta\mathbf{T}^{F107}$ monotonically increases with altitude
750 due to the fact that the solar UV fluxes of greater variations at shorter wavelengths are generally
751 absorbed at higher altitudes. The two periods used to derive the statistical equilibrium states are
752 2002-2003 and 2008-2009, corresponding to near solar maximum and solar minimum,
753 respectively. The CO_2 mixing ratio between these two periods increases from ~374.7 ppmv to
754 ~386.3 ppmv. It is consistently found by both datasets that for a half cycle span of the 11-year
755 solar cycle the largest component of the partial temperature changes ($\Delta\mathbf{T}^{(n)}$) in the middle
756 atmosphere is the one due to the variation of the input solar flux ($\Delta\mathbf{T}^{F107}$). The effect of
757 increasing CO_2 always cools the middle atmosphere with time ($\Delta\mathbf{T}^{CO2}<0$). On the other hand,
758 depending on the relative importance of O_3 heating and cooling rates, $\Delta\mathbf{T}^{O3}$ could be either
759 positive or negative. The MCFRAM analysis to GEOSCCM fields suggests that $\Delta\mathbf{T}^{H2O}$ makes a
760 minor contribution to the total temperature change observed from the atmosphere ($\Delta\mathbf{T}^{total}$). The
761 partial temperature change due to the variation of the effective albedo of the surface and lower
762 atmosphere to the solar radiation ($\Delta\mathbf{T}^{\omega 0}$) is negligibly small in comparison with those by other
763 factors.

Because of the lack of all the required parameters in the input datasets, the partial temperature change due to non-radiative processes ($\Delta\mathbf{T}^{non-rad}$) often needs to be evaluated by either an energy or a temperature residual approach. Such an approach is well-founded due to the existence of the additive property for the generic energy equation (3) or the basic MCFRAM equation (10) to temperature changes. $\Delta\mathbf{T}^{non-rad}$ for the SABER measurements includes all dynamical effects whereas three individual components in $\Delta\mathbf{T}^{non-rad}$ can be evaluated separately based on the GEOSCCM model outputs. In both cases, the typical magnitude of $\Delta\mathbf{T}^{non-rad}$ is significantly greater than any component consisting of partial temperature changes due to radiation processes ($\Delta\mathbf{T}^{rad}$). However, the global average of $\Delta\mathbf{T}^{non-rad}$ is much smaller than that of $\Delta\mathbf{T}^{rad}$ below ~70 km, indicating the lack of vertical transport of energy by eddies or by global mean vertical velocity. Physically, this means that the globally averaged climate change in the middle atmosphere below ~70 km is thermally driven. This also means that the globally averaged partial temperature change due to all radiative processes is approximately equal to the observed temperature change. It ranges from −0.5 K near 25 km to −1.0 K near 70 km from the near solar maximum to the solar minimum.

ACKNOWLEDGMENTS

This research was supported by NASA Living With a Star Program under Grant NNX13AF91G and NASA Geospace Science Program under Grant NNX13AE33G to The Johns Hopkins University Applied Physics Laboratory. Constructive comments from Jae N. Lee on the original manuscript are greatly appreciated.

786 **REFERENCES:**

787 Aquila, V., L. D. Oman, R. S. Stolarski, P. R. Colarco, and P. A. Newman, 2012: Dispersion of
788 the volcanic sulfate cloud from a Mount Pinatubo–like eruption. *J. Geophys. Res.*, **117**,
789 D06216. doi:10.1029/2011JD016968.

790 Aquila, V., L. D. Oman, R. S. Stolarski, A. R. Douglass, and P. A. Newman, 2013: The response
791 of ozone and nitrogen dioxide to the eruption of Mt. Pinatubo at southern and northern
792 midlatitudes. *J. Atmos. Sci.*, **70**, 894–900. doi:10.1175/JAS-D-12-0143.1.

793 Banks, P. M. and G. Kockarts, 1973: *Aeronomy, Part B.* Academic Press, New York, 355 pp.

794 Butchart, N., *et al*., 2006: Simulations of anthropogenic change in the strength of the Brewer-
795 Dobson circulation. *Climate Dyn*., **27**, 727-741.

796 Cai, M., and J. Lu, 2009: A new framework for isolating individual feedback processes in
797 coupled general circulation climate models. Part II: Method demonstrations and
798 comparisons. *Climate Dyn*., **32**, 887-900, doi: 10.1007/s00382-008-0424-4.

799 Cogley, A. C., and W. J. Borucki, 1976: Exponential approximation for daily average solar
800 heating or photolysis. *J. Atmos. Sci*., **33**, 1347-1356.

801 Douglass, A. R., C. J. Weaver, R. B. Rood, and L. Coy, 1996: A three-dimensional simulation of
802 the ozone annual cycle using winds from a data assimilation system, *J. Geophys. Res*., **101**,
803 1463-1474.

804 Fels, S. B., 1982: A parameterization of scale-dependent radiative damping rates in the middle
805 atmosphere. *J. Atmos. Sci*., **39**, 1141-1152.

806 Fels, S. B., 1987: Response of the middle atmosphere to changing O_3 and CO_2 – A speculative
807 tutorial. In *Transport Processes in the Middle Atmosphere*, G. Visconti and R. Garcia
808 (Eds.), pp. 371-386, D. Reidel, Boston, MA.

809 Garcia, R. R., and W. J. Randel, 2008: Acceleration of the Brewer-Dobson circulation due to
810 increases in greenhouse gases. *J. Atmos. Sci.*, **65**, 2731-2739.

811 Goody, R. M., and Y. L. Yung, 1989: *Atmospheric Radiation: Theoretical Basis. Second Edition*.
812 Oxford Univ. Press, New York and Oxford, 519 pp.
813 Holton, J. R., 2004: *An Introduction to Dynamic Meteorology, Fourth Edition*, Elsevier
814 Academic Press, New York, 535 pp.
815 Kiehl, J. T., and S. Solomon, 1986: On the radiative balance of the stratosphere. *J. Atmos. Sci*.,
816 **43**, 1525-1534.
817 Kutepov, A. A., A. G. Feofilov, B. T. Marshall, L. L. Gordley, W. D. Pesnell, R. A. Goldberg,
818 and J. M. Russell III, 2006: SABER temperature observations in the summer polar
819 mesosphere and lower thermosphere: Importance of accounting for the CO_2 ν_2 quanta V-V
820 exchange, *Geophys. Res. Lett.,* **33**, L21809, doi:10.1029/2006GL026591.
821 Lean, J., 1991: Variations in the Sun's radiative output. *Rev. Geophys*., **29**, 505-535.
822 Liou, K. N., 2002: *An Introduction to Atmospheric Radiation.* 2nd Edition. Academic Press, New
823 York, 583 pp.
824 Lu, J., and M. Cai, 2009: A new framework for isolating individual feedback processes in
825 coupled general circulation climate models. Part I: Formulation. *Climate Dyn*., **32**, 873-
826 885, doi: 10.1007/s00382-008-0425-3.
827 Lu, J. and M. Cai, 2010: Quantifying contributions to polar warming amplification in an
828 idealized coupled general circulation model. *Clim. Dyn*., **34**, 449-687.
829 Lubken, F. -J, 1999: Thermal structure of the Arctic summer mesosphere. *J. Geophys. Res.*, **104**
830 (D8), 9135-9149.
831 Lubken, F. -J, M. J. Jarvis, G. O. L. Jones, 1999: First in situ temperature measurements at the
832 Antarctic summer mesopause. *Geophys. Res. Lett*., 26, 3581-3584.
833 Meier, R. R., D. E. Anderson, M. Nicolet, 1982: Radiation field in the troposphere and
834 stratosphere from 240 to 1000 nm. I. General analysis. *Planet. Space Sci*., **30**, 923-933.

835 Molod, A., L. Takacs, M. Suarez, J. Bacmeister, I.-S. Song, and A. Eichmann, 2012: The GEOS-
836 5 Atmospheric General Circulation Model: Mean climate and development from MERRA
837 to Fortuna, Technical Report Series on Global Modeling and Data Assimilation, 28,
838 NASA, Greenbelt, Md.
839 Nicolet, M., R. R. Meier, and D. E. Anderson, 1982: Radiation field in the troposphere and
840 stratosphere from 240 to 1000 nm. II. Numerical analysis. *Planet. Space Sci*., **30**, 935-983.
841 Olaguer, E. P., H. Yang, and K. K. Tung, 1992: A reexamination of the radiative balance of the
842 stratosphere. *J. Atmos. Sci*., **49**, 1242-1263.
843 Pawson, S., *et al*., 2008: Goddard Earth Observing System Chemistry-Climate Model
844 simulations of stratospheric ozone-temperature coupling between 1950 and 2005, *J.*
845 *Geophys. Res*., **113**, D12103, doi:10.1029/2007JD009511.
846 Rees, M. H., 1989: *Physics and Chemistry of the Upper Atmosphere***.** Cambridge Univ. Press,
847 289 pp.
848 Rienecker, M.M., M.J. Suarez, R. Todling, J. Bacmeister, L. Takacs, H.-C. Liu, W. Gu, M.
849 Sienkiewicz, R.D. Koster,R. Gelaro, I. Stajner, and J.E. Nielsen, The GEOS-5 data
850 assimilation system - documentation of versions 5.0.1, 5.1.0, and 5.2.0. NASA Technical
851 Report Series on Global Modeling and Data Assimilation, M. J. Suarez ed., NASA/TM–
852 2008–104606, Vol. **27**, 101 pp, 2008: downloadable at http://gmao.gsfc.nasa.gov/systems/
853 geos5/index_arch.php.
854 Russell III, J. M., M. G. Mlynczak, L. L. Gordley, J. Tansock, and R. Esplin, 1999: An overview
855 of the SAVER experiment and preliminary calibration results, *Proc. SPIE*, **3756**,
856 doi:10.1117/12.366382, 277-288.
857 Sejas, S., M. Cai, A. Hu, G. A. Meehl, W. Washington, and P. Taylor, 2014: Individual feedback
858 contributions to the seasonality of surface warming. *J. Climate*, doi:10.1175/JCLI-D-13-
859 00658.1, in press.

860 Shepherd, T. G., and C. McLandress, 2011: A robust mechanism for strengtherning of the
861 Brewer-Dobson circulation in response to climate change: Critical-layer control of
862 subtropical wave breaking. *J. Atmos. Sci.*, **68**, 784-797.
863 Soden, B. J., I. M. Held, R. Colman, K. M. Shell, J. T. Kiehl, and C. A. Shields, 2008:
864 Quantifying climate feedbacks using radiative kernels. *J. Climate*, **21**, 3504-3520.
865 Solomon, S., K. Rosenlof, R. W. Portmann, J. S. Daniel, S. Davis, T. J. Sanford, and G. Plattner,
866 2010: Contributions of stratospheric water vapor to decadal changes in the rate of global
867 warming, *Science*, **327**, 1219-1223.
868 Song, X., G. J. Zhang, and Ming Cai, 2014: Characterizing the climate feedback pattern in the
869 NCAR CCSM3-SOM using hourly data. *J. Climate*, **27**, 2912–2930.
870 Swartz, W. H., R. S. Stolarski, L. D. Oman, E. L. Fleming, and C. H. Jackman, 2012: Middle
871 atmosphere response to different descritptions of the 11-yr solar cycle in spectral irradiance
872 in a chemistry-climate model. *Atmos. Chem. Phys*., **12**, 5937-5948.
873 Taylor, P. C., M. Cai, A. Hu, G. A. Meehl, W. Washington, and G. J. Zhang, 2013: A
874 decomposition of feedback contributions to polar warming amplification. *J. Climate*, **26**,
875 7023-7043.
876 Zhu, X., 1993: Radiative damping revisited: Parameterization of damping rate in the middle
877 atmosphere. *J. Atmos. Sci.*, **50**, 3008-3021.
878 Zhu, X., 1994: An accurate and efficient radiation algorithm for middle atmosphere models. *J.*
879 *Atmos. Sci*., **51**, 3593-3614.
880 Zhu, X., 2004: Radiative transfer in the middle atmosphere and planetary atmospheres. In
881 "*Observation, Theory and Modeling of Atmospheric Variability*" (*X. Zhu et al*., eds.), pp.
882 359-396. World Scientific Pub. Co., Singapore.
883 Zhu, X., and D. F. Strobel, 1991: Radiative damping in the upper mesosphere. *J. Atmos. Sci.*, **48**,
884 184-199.

885 Zhu, X., M. E. Summers, and D. F. Strobel, 1991: Analytic models for the ozone radiative
886 absorption rate at 9.6 μm in the mesosphere. *J. Geophys. Res.*, **96**(D10), 18,551-18,559.
887 Zhu, X., M. E. Summers, and D. F. Strobel, 1992: Calculation of CO_2 15 μm band atmospheric
888 cooling rates by Curtis matrix interpolation of correlated-k coefficients. *J. Geophys. Res.*,
889 **97**(D12), 12,787-12,797.
890 Zhu, X., J.-H. Yee, and E. R. Talaat, 2001: Diagnosis of dynamics and energy balance in the
891 mesosphere and lower thermosphere. *J. Atmos. Sci*., **58**, 2441-2454.
892 Zhu, X., J.-H. Yee, S. A. Lloyd, and D. F. Strobel, 1999: Numerical modeling of chemical-
893 dynamical coupling in the upper stratosphere and mesosphere. *J. Geophys. Res.*, **104** (D19),
894 23,995–24,011.
895 Zhu, X., D. F., Strobel, M. F. Flasar, 2008: Exchange of global mean angular momentum
896 between an atmosphere and its underlying planet. *Planet. Space Sci*., 56, 1524-1531.
897 Zhu, X., J.-H. Yee, W. H. Swartz, E. R. Talaat and L. Coy, 2010: A spectral parameterization of
898 drag, eddy diffusion and wave heating for a three-dimensional flow induced by breaking
899 gravity waves. *J. Atmos. Sci.*, **67**, 2520–2536.
900 Zhu, X., D. F. Strobel, and J. T. Erwin, 2014: The density and thermal structure of Pluto's
901 atmosphere and associated escape processes and rates. *Icarus*, **228**, 301-314.
902

903

904

905 Table 1. Partial temperature changes ($\Delta\mathbf{T}^{(n)}$) and their physical meanings

$\Delta\mathbf{T}^{(n)}$	**Definitions**	**Physical meanings of partial temperature changes**
$\Delta\mathbf{T}^{\mathrm{CO2}}$	$\mathbf{Z}\cdot(-\Delta\mathbf{R}^{\mathrm{CO2}})$	$\Delta\mathbf{T}^{(1)}$ due to changes in CO_2
$\Delta\mathbf{T}^{\mathrm{O3}}$	$\mathbf{Z}\cdot(\Delta\mathbf{S}^{\mathrm{O3}}-\Delta\mathbf{R}^{\mathrm{O3}})$	$\Delta\mathbf{T}^{(2)}$ due to changes in O_3
$\Delta\mathbf{T}^{\mathrm{F107}}$	$\mathbf{Z}\cdot\Delta\mathbf{S}^{\mathrm{F107}}$	$\Delta\mathbf{T}^{(3)}$ due to change in downward solar radiation at TOA
$\Delta\mathbf{T}^{\mathrm{H2O}}$	$\mathbf{Z}\cdot(-\Delta\mathbf{R}^{\mathrm{H2O}})$	$\Delta\mathbf{T}^{(4)}$ due to changes in H_2O
$\Delta\mathbf{T}^{\mathrm{O2}}$	$\mathbf{Z}\cdot\Delta\mathbf{S}^{\mathrm{O2}}$	$\Delta\mathbf{T}^{(5)}$ due to changes in O_2
$\Delta\mathbf{T}^{\omega 0}$	$\mathbf{Z}\cdot\Delta\mathbf{S}^{\omega 0}$	$\Delta\mathbf{T}^{(6)}$ due to changes in troposphere albedo to the solar radiation
$\Delta\mathbf{T}^{w^*}$	$\mathbf{Z}\cdot(\boldsymbol{\Theta}\Delta\mathbf{w}^*)$	$\Delta\mathbf{T}^{(7)}$ due to changes in the resolved vertical velocity
$\Delta\mathbf{T}^{\Theta}$	$\mathbf{Z}\cdot(\Delta\boldsymbol{\Theta})\mathbf{w}^*$	$\Delta\mathbf{T}^{(8)}$ due to changes in the static stability
$\Delta\mathbf{T}^{eddy}$	$\mathbf{Z}\cdot(\Delta''\mathbf{Q}^{eddy})$	$\Delta\mathbf{T}^{(9)}$ due to changes in the un-resolved eddies
$\Delta\mathbf{T}^{non-rad}$	$\mathbf{Z}\cdot(\Delta\mathbf{R}-\Delta\mathbf{Q}_{mol}-\Delta\mathbf{S})$	$\Delta\mathbf{T}^{(7-9)}$ due to changes in circulation

906

907

908

909

910 FIGURE CAPTIONS

911

912 Figure 1. Global mean temperature and ozone profiles in the middle atmosphere derived from
913 TIMED/SABER measurements in the low and mid-latitudes over a 12-year period of 2002-2013.
914 The TIMED/SABER measurements in the middle atmosphere are merged to the US Standard
915 Atmosphere in the troposphere. The vertical resolution is about 0.7 km.

916

917 Figure 2. Selected vertical eigenmodes of the generalized damping matrix A calculated from *T*
918 and O_3 shown in Fig. 1 based on the JHU/APL radiation algorithm. The CO_2 volume mixing
919 ratio is set at 2005 level of 380 ppmv. The unit of the eigenvalues shown in the figure boxes is
920 day^{-1}.

921

922 Figure 3. A quantitative relationship between the generalized damping rate and the vertical
923 wavenumber at which the poser spectral density is maximally peaked. Also shown in the figure
924 are analytic fits of radiative damping given by (Zhu 1993) and a fit for diffusive damping
925 proportional to the square of the vertical wavenumber.

926

927 Figure 4. Linear temperature responses to three energy perturbations caused by changing three
928 atmospheric parameters (i) CO_2 volume mixing ratio is doubled from 380 ppmv to 760 ppmv,
929 (ii) O_3 mixing ratio is uniformly reduced by 50%, and (iii) solar flux index $F_{10.7}$ is increased
930 from 60 to 260 (in units of 10^{-22} W $m^{-2}Hz^{-1}$).

931

932 Figure 5. Zonal mean *T* and O_3 fields averaged over a 12-year period of 2002-2013 and their
933 differences between two equilibrium states covering the periods of 2002-2003 and 2008-2009,
934 respectively.

935

936 Figure 6. Two dimensional distributions of partial temperature changes between two time
937 periods of 2002-2003 and 2008-2009 due to variations in (a) CO_2, (b) O_3, (c) $F_{10.7}$, and (d)
938 atmospheric circulation, respectively. (e) Equivalent partial change in vertical velocity due to

939 change in CO_2. (f) Error in partial temperature change of non-radiative processes due to
940 linearization approximation.
941
942 Figure 7. Globally averaged partial temperature changes $\Delta\mathbf{T}^{CO2}$ (dashed line with squares),
943 $\Delta\mathbf{T}^{O3}$ (dashed line with triangles), $\Delta\mathbf{T}^{F107}$ (dashed line with circles) and their sum approximately
944 representing $\Delta\mathbf{T}^{rad}$ (solid line with solid circles). (b) Globally averaged total temperature change
945 $\Delta\mathbf{T}^{total}$ (dashed line) and partial temperature changes $\Delta\mathbf{T}^{rad}$ (solid line with solid circles) and
946 $\Delta\mathbf{T}^{non-rad}$ (solid line with diamonds).
947
948 Figure 8. Changes in effective albedo of the surface and lower atmosphere scaled by the
949 diurnally averaged solar radiation between 2002-2003 and 2008-2009.
950
951 Figure 9. Partial temperature changes caused by various energy perturbation components in the
952 middle atmosphere. The unit in scale bars of all panels is K.
953
954 Figure 10. Globally averaged partial temperature changes shown in Fig. 9.
955
956

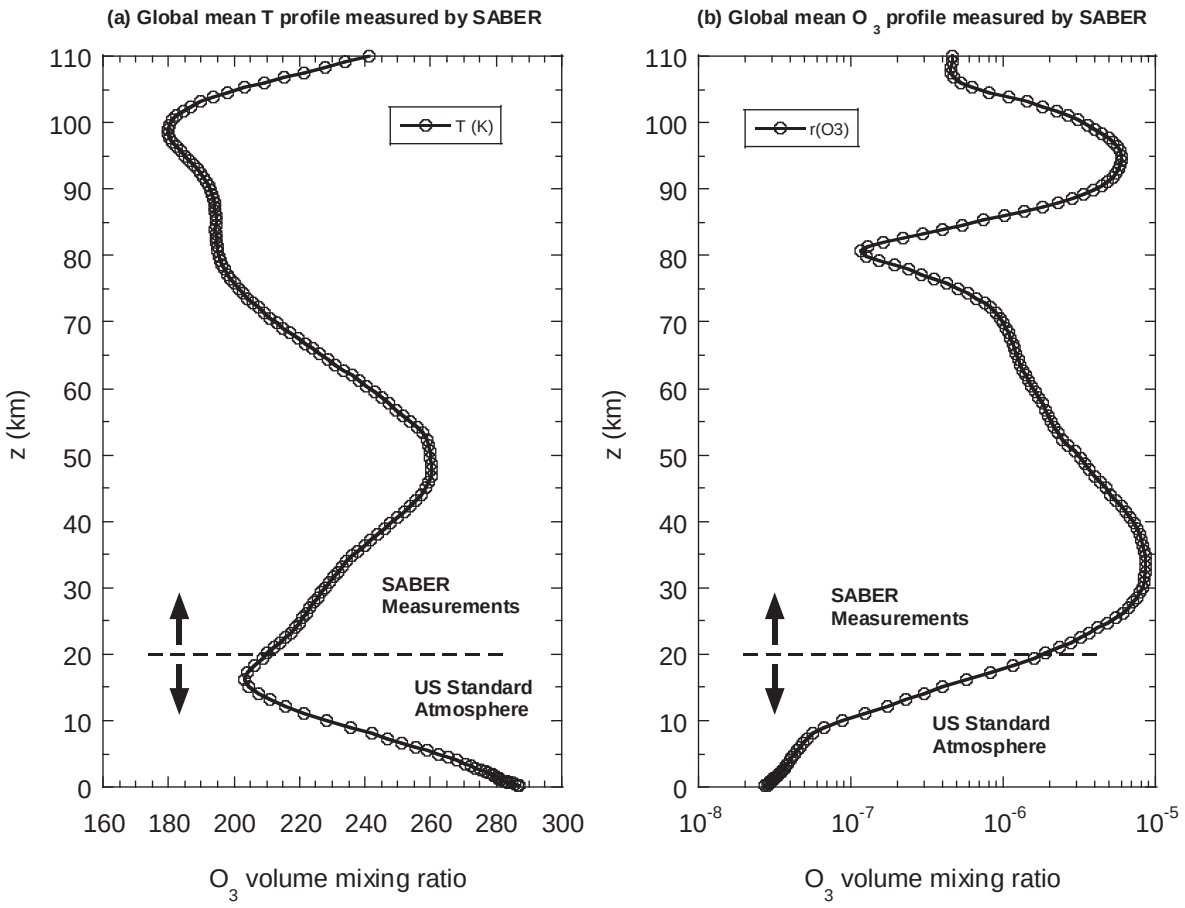

Figure 1. Global mean temperature and ozone profiles in the middle atmosphere derived from TIMED/SABER measurements in the low and mid-latitudes over a 12-year period of 2002-2013. The TIMED/SABER measurements in the middle atmosphere are merged to the US Standard Atmosphere in the troposphere. The vertical resolution is about 0.7 km.

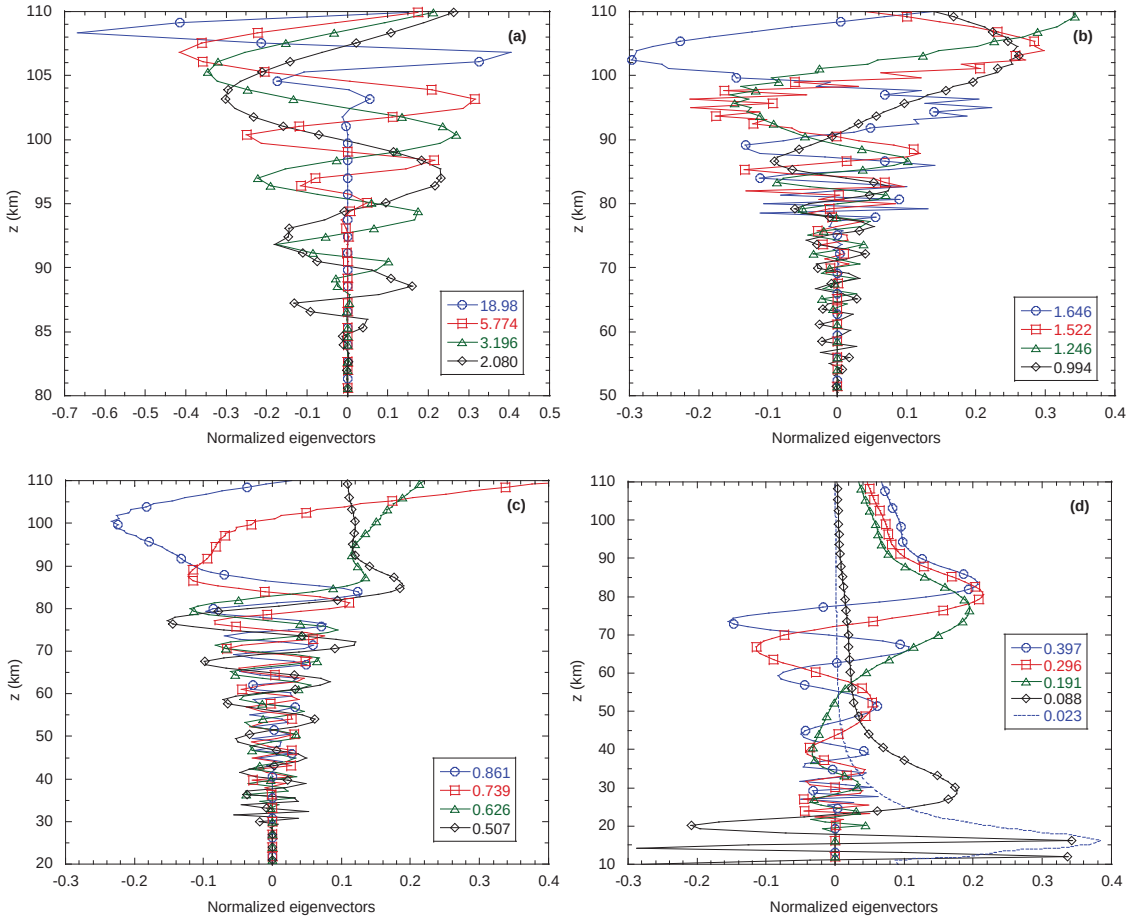

Figure 2. Selected vertical eigenmodes of the generalized damping matrix **A** calculated from T and O_3 shown in Fig. 1 based on the JHU/APL radiation algorithm. The CO_2 volume mixing ratio is set at 2005 level of 380 ppmv. The unit of the eigenvalues shown in the figure boxes is day^{-1}.

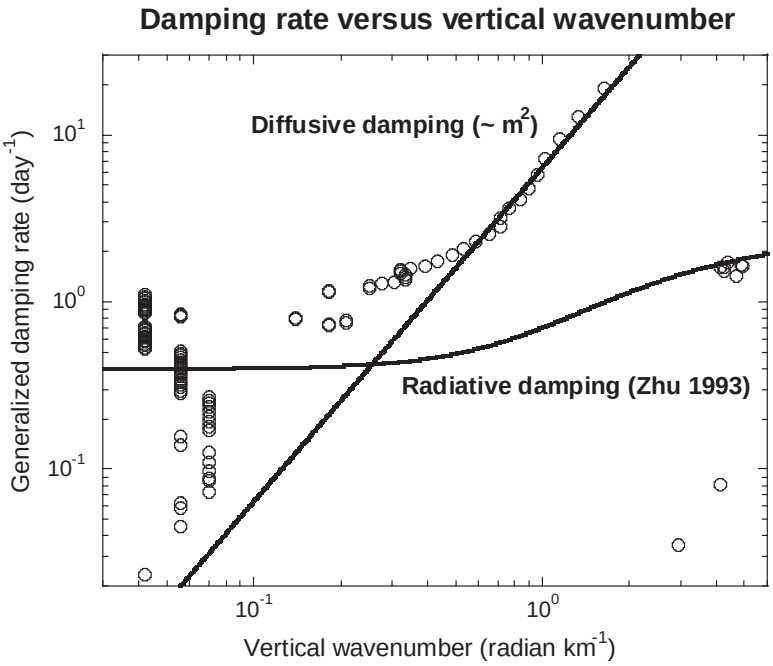

Figure 3. A quantitative relationship between the generalized damping rate and the vertical wavenumber at which the poser spectral density is maximally peaked. Also shown in the figure are analytic fits of radiative damping given by (Zhu 1993) and a fit for diffusive damping proportional to the square of the vertical wavenumber.

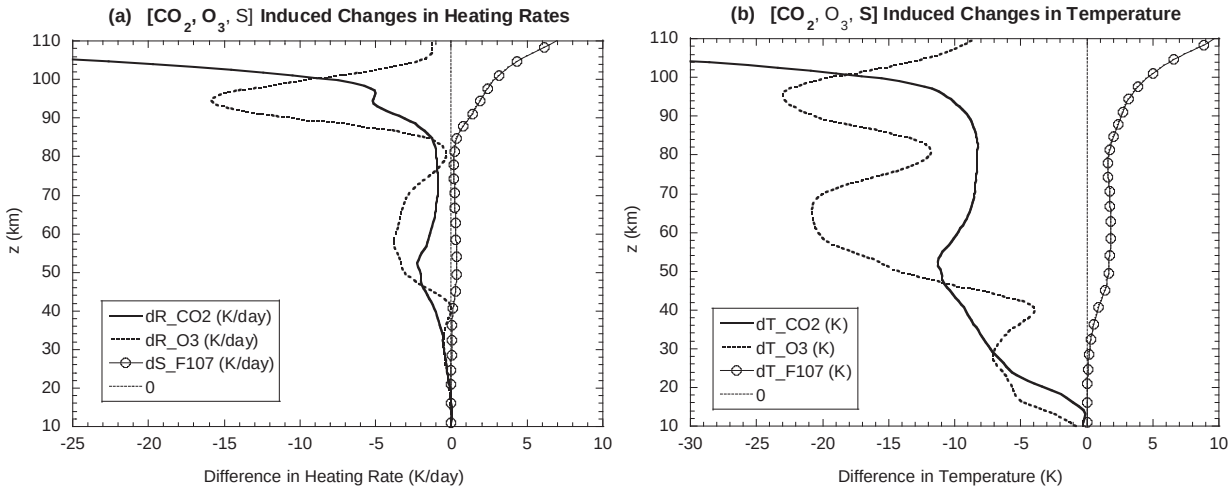

Figure 4. Linear temperature responses to three energy perturbations caused by changing three atmospheric parameters (i) CO_2 volume mixing ratio is doubled from 380 ppmv to 760 ppmv, (ii) O_3 mixing ratio is uniformly reduced by 50%, and (iii) solar flux index $F_{10.7}$ is increased from 60 to 260 (in units of 10^{-22} W m^{-2}Hz^{-1}).

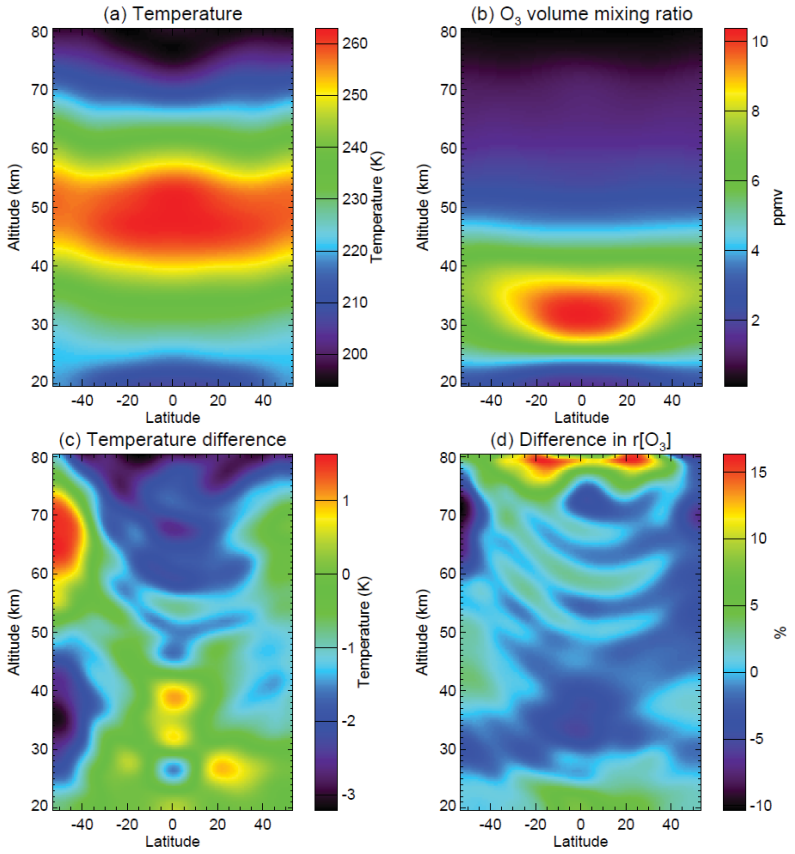

997

998
999

1000 Figure 5. Zonal mean *T* and O_3 fields averaged over a 12-year period of 2002-2013 and
1001 their differences between two equilibrium states covering the periods of 2002-2003 and
1002 2008-2009, respectively.

1003

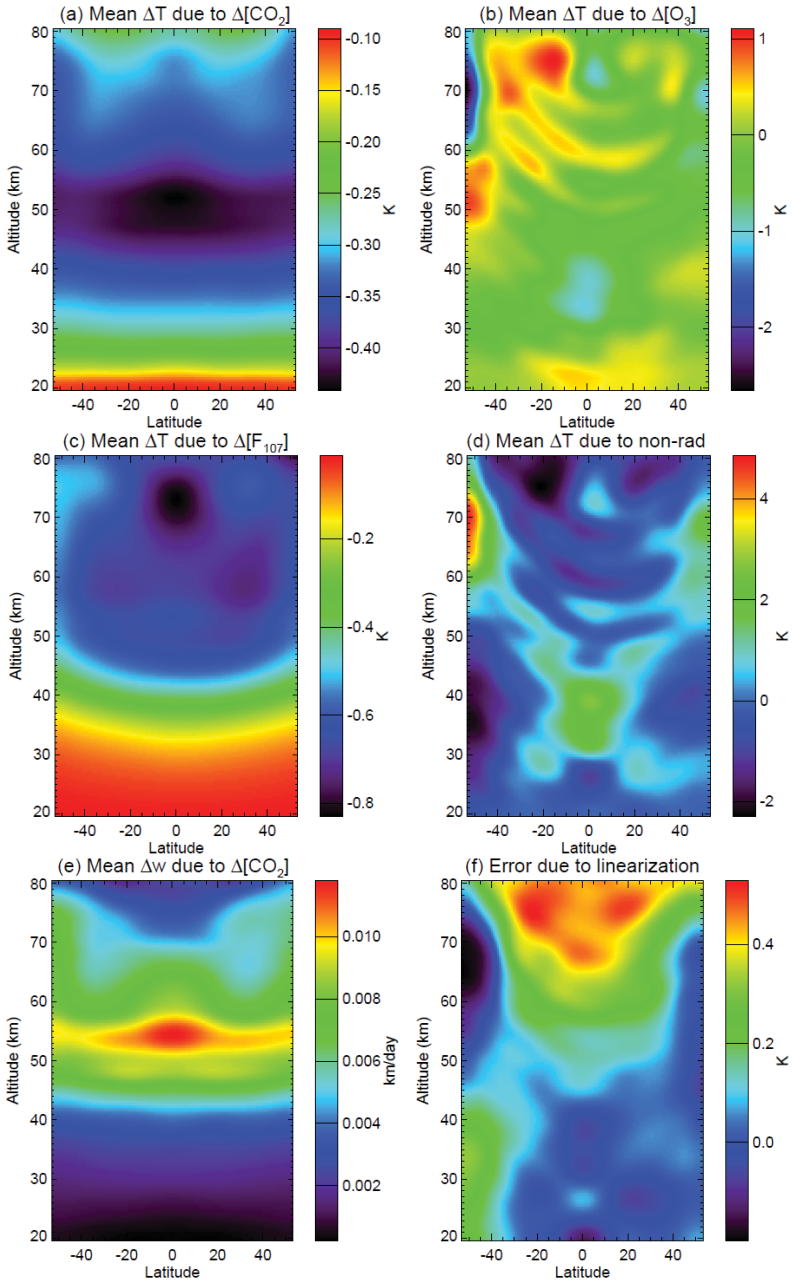

Figure 6. Two dimensional distributions of partial temperature changes between two time periods of 2002-2003 and 2008-2009 due to variations in (a) CO_2, (b) O_3, (c) $F_{10.7}$, and (d) atmospheric circulation, respectively. (e) Equivalent partial change in vertical velocity due to change in CO_2. (f) Error in partial temperature change of non-radiative processes due to linearization approximation.

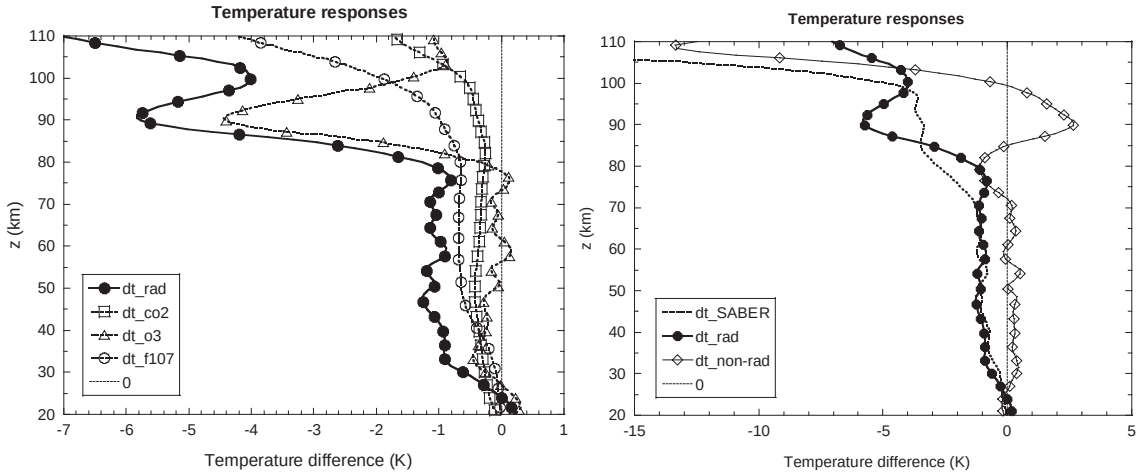

Figure 7. (a) Globally averaged partial temperature changes $\Delta\mathbf{T}^{CO2}$ (dashed line with squares), $\Delta\mathbf{T}^{O3}$ (dashed line with triangles), $\Delta\mathbf{T}^{F107}$ (dashed line with circles) and their sum approximately representing $\Delta\mathbf{T}^{rad}$ (solid line with solid circles). (b) Globally averaged total temperature change $\Delta\mathbf{T}^{total}$ (dashed line) and partial temperature changes $\Delta\mathbf{T}^{rad}$ (solid line with solid circles) and $\Delta\mathbf{T}^{non-rad}$ (solid line with diamonds).

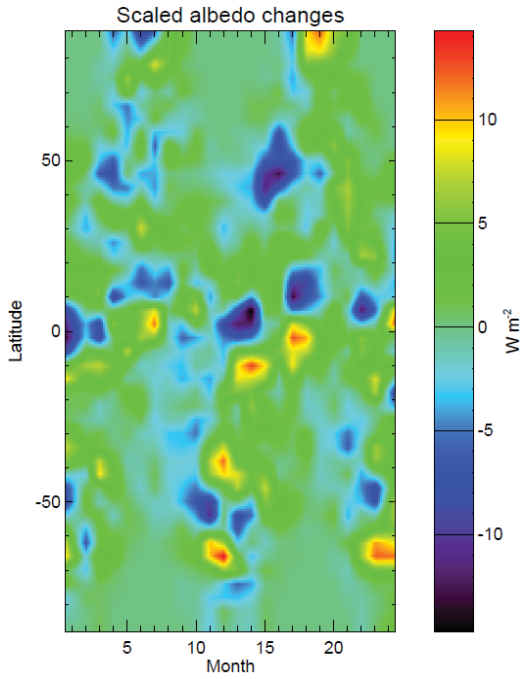

Figure 8. Changes in effective albedo of the surface and lower atmosphere scaled by the diurnally averaged solar radiation between 2002-2003 and 2008-2009.

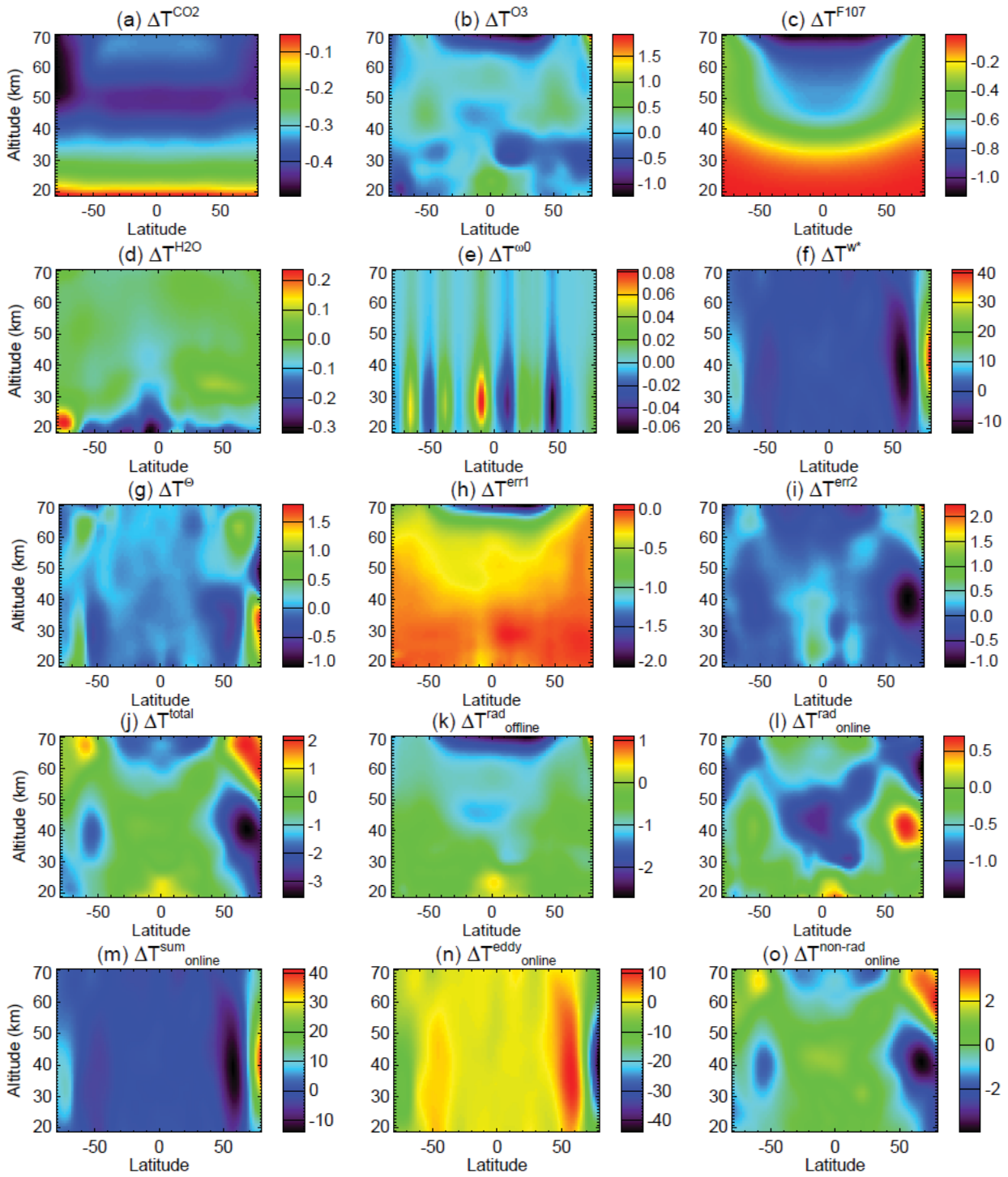

Figure 9. Partial temperature changes caused by various energy perturbation components in the middle atmosphere. The unit in scale bars of all panels is K.

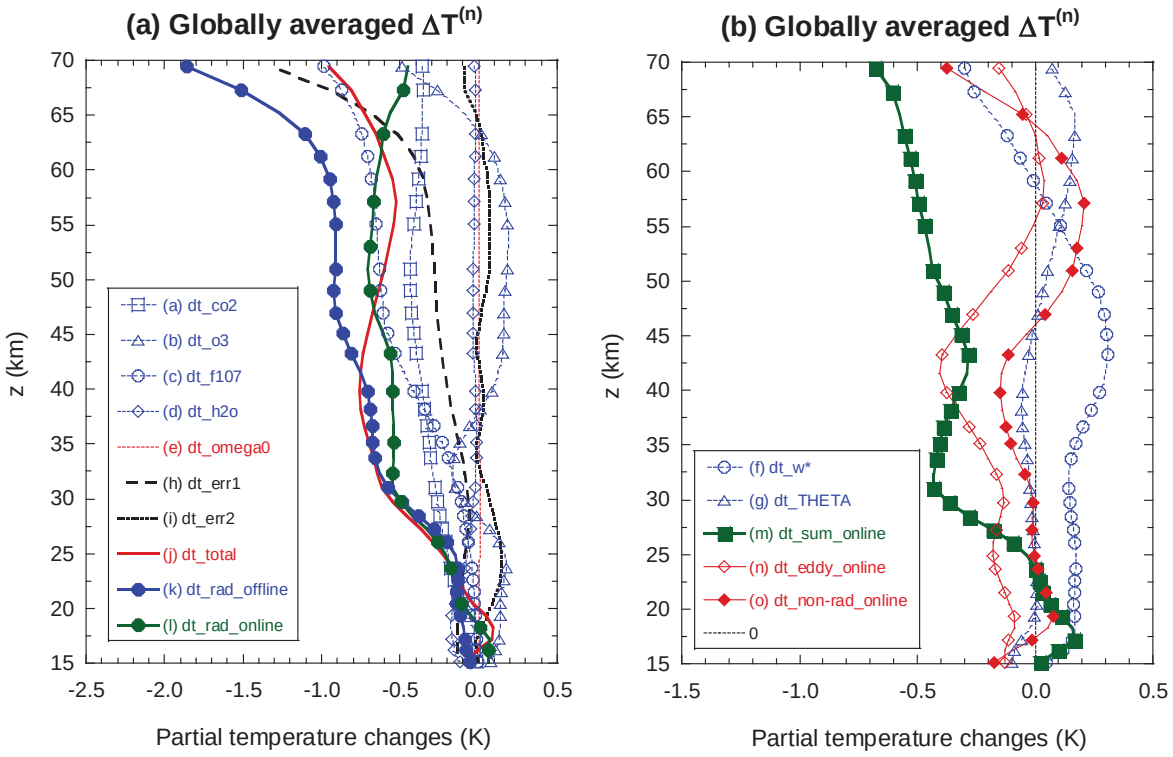

Figure 10. Globally averaged partial temperature changes shown in Fig. 9.